INTERFACE REACTION INDUCED STRESS DEVELOPMENT IN AN ALUMINUM THIN FILM COPPER BULK PLATE DIFFUSION COUPLE

BY

MICHAEL CODIE MISHLER

Presented to the Faculty of the Graduate School of

The University of Texas at Arlington in Partial Fulfillment

of the Requirements

for the Degree of

MASTER OF SCIENCE IN MATERIALS SCIENCE & ENGINEERING

THE UNIVERSITY OF TEXAS AT ARLINGTON

DECEMBER 2015

Acknowledgements

There could be no acknowledgement here if I didn't begin by recognizing my wonderful wife Janet Mishler. Without her support, I would not have been able to return to school to achieve this degree. I would also like to thank Eva Lou Sheffield for setting me on the path of learning at such an early age. I would like to thank William Cecile Watson for encouraging me to explore all things. I would like to thank Cora Mishler for being the example that it can be done against all odds.

I would like to give special thanks to my research advisor Dr. Choong-Un Kim for his guidance in my research and patience towards unforeseen mishaps along the way. His knowledge and understanding of the subject is what attracted me to his research group and I cannot imagine a better match for having completed this degree.

I would also like to extend my appreciation to Dr. Yaowu Hao for working with me during my admission to the department under non-standard circumstances. I would like to thank Dr. Minyoung Kim, for assistance beyond expectations. Special thanks to my peer students in Professor Kim's research group for their assistance and comradery. Thank you to the faculty and staff of the Material Science & Engineering department, extended family and friends for their continued support.

Abstract

INTERFACE REACTION INDUCED STRESS DEVELOPMENT IN AN ALUMINUM THIN FILM COPPER BULK PLATE DIFFUSION COUPLE

Michael Codie Mishler, MS

The University of Texas at Arlington, 2015

Supervising professor: Choong-Un Kim

This thesis investigates the mechanism of the interface reaction induced intermetallic compound (IMC) phase formation and its impact on the interface reliability in the Al-Cu diffusion couple. This study is motivated by the accelerated failure experiments in lead frame to integrated circuit (IC) package wire-bonds using copper (Cu) wire and aluminum (Al) bond-pad that have shown failure most often occurs at the interface of the IMC γ_2-phase (Cu_9Al_4).

In a simulative investigation, we created a diffusion couple consisting of Cu bulk plate coated with pure Al thin film ~2μm thick. This configuration resembles the microstructural configuration of a Cu wire / Al bond pad. In addition, we introduce two types of Cu plate as our samples, namely half-hard and fully annealed Cu plate. These samples are introduced in order to investigate the effect of microstructure, such as dislocation and grain boundaries and also residual stress on the interface reaction kinetics.

Our experiment of Al thin film on bulk Cu has shown that the interface reaction creates a tensile stress in the Cu lattice. The stress generation is found to be closely

associated with the formation of γ_2-phase. The expected initial formation of θ-phase ($CuAl_2$) is never seen in our experiment as has been reported in thin-film / thin-film (TF/TF) and bulk / bulk (B/B) diffusion couples. While the principle mechanism of stress generation in Cu plate with the IMC formation remains the same for both half-hard and fully annealed Cu plate, X-ray diffraction data collected on aged samples revealed that the rate of IMC formation and thus the stress generation is smaller in half-hard Cu. This is the opposite of what is expected. The presence of finer grains and high dislocation density should promote short-circuit diffusion making the diffusion of Cu into Al faster. It is our conclusion that the enhancement in the short-circuit diffusion is outweighed by a suppression of diffusion by compressive residual stress in the half-hard Cu. Half-hard Cu plate is expected to have compressive residual stress and therefore likely to contain lower equilibrium concentration of vacancies.

Our results of the stress generation during γ_2-phase formation and the suppression of diffusion in compressively strained lattices explains why it has been observed that IMC formation occurs first near the outer edges of the wire-bonds. The wire-bonding process creates a work hardened condition towards the center of the wire-bond, slowing IMC formation. The interface stress created by γ_2-phase formation expanding the Cu lattice presents favorable conditions for crack nucleation which has been observed in Cu-Al wire-bond failure.

Table of Contents

List of Figures

List of Tables

Chapter 1

Introduction and Background

1.1 Research background of Intermetallic Compounds (IMC)

1.1.1 Motivations for study

As the microelectronics industry investigates new methods and materials to accommodate the ever decreasing node size, copper wire has been considered for replacing gold wire in wire-bonds that attach integrated circuit (IC) packages to lead boards[26, 28]. Copper has many advantages over gold wire and disadvantages that previously made copper cost prohibitive have now been offset by the rising price of gold. The rising price of gold was not foreseen by the industry, so the failure kinetics of copper wire-bonds were only minimally investigated. The need now exists to fully investigate this understudied field.

The mainstream metal used in IC packages is aluminum. This study focuses on the connection of copper (Cu) wire-bonds to aluminum (Al) bond-pads on the IC. A cross-reference study of literature will show that failure in the Cu wire – Al bond pad interface occurs at boundaries where the Hume-Rothery γ_2-phase intermetallic compound (IMC) exists. Associated research in our lab has verified this; see Figure 2-4. Typically, the articles call this detail out but fail to produce convincing conclusions or evidence as to why the failure is associated with this particular phase. It is therefore prudent, if one is to understand the nature of the failure, to understand the properties and behavior of this particular IMC phase.

Five IMC's have been shown to exist in the Cu-Al system[29]. Studies of Cu-Al IMC's date back to the 1930's[7] with concentrations in the areas of formation energies (highly contested)[29], formation sequence (contested)[27,29], IMC crystal structure (reasonably established)[9], and interface structure (few articles)[28]. There are numerous papers that have investigated the

overall IMC formation kinetics and lesser still on the individual IMC's[29-44]. The typical assumptions in the literature is that bulk thermal diffusion dominates in the diffusion couple[23, 29]. Interface structure with respect to IMC's has been investigated in the roll bonded interface[23], bilayer thin film[29] but not in ratios where a thin film is coupled with bulk quantities of the counterpart constituent. In the upcoming microelectronic node size generations, the quantity of wire vs bond pad ratio would constitute a bulk / thin film interface. Careful review of many studies reveals that cracks and voids typically nucleate at interfaces where γ_2-phase is one of the boundaries. As the γ_2-phase exists near the saturation limit of Al in Cu, the possibility of failures associated with this phase become more probable. To the limit of my search, interface structure kinetics, with respect to γ_2-phase, has not been studied.

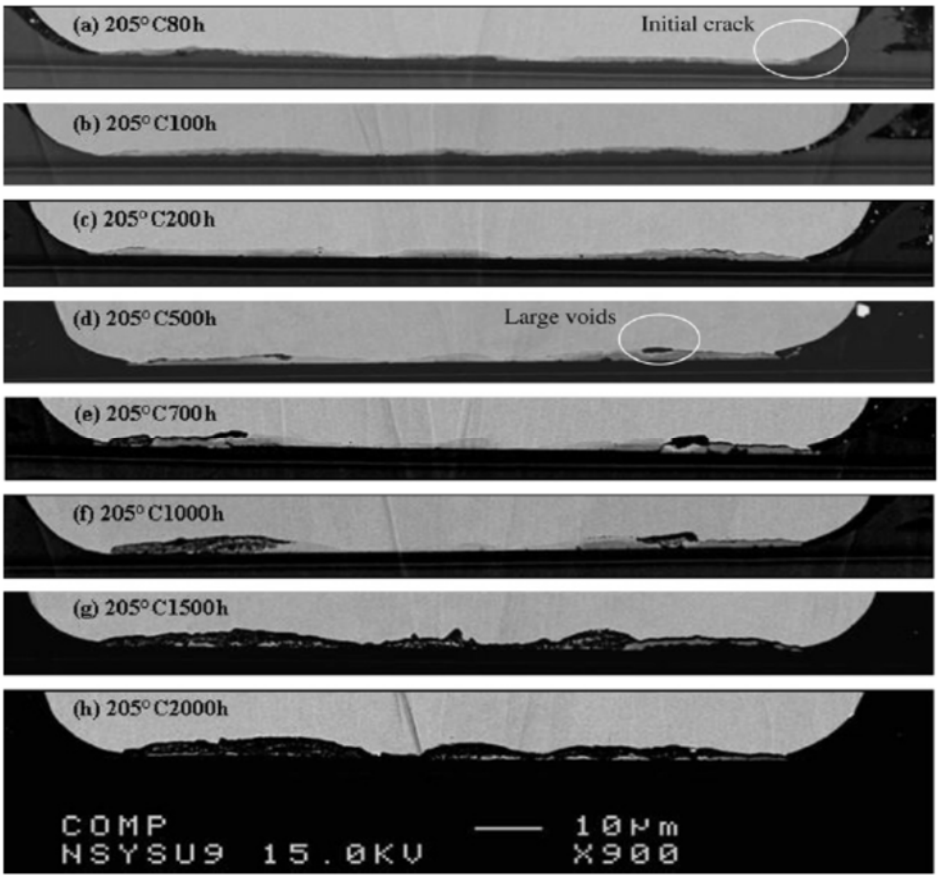

Figure 1: Copper Wire, Aluminum bond pad failure example[1]

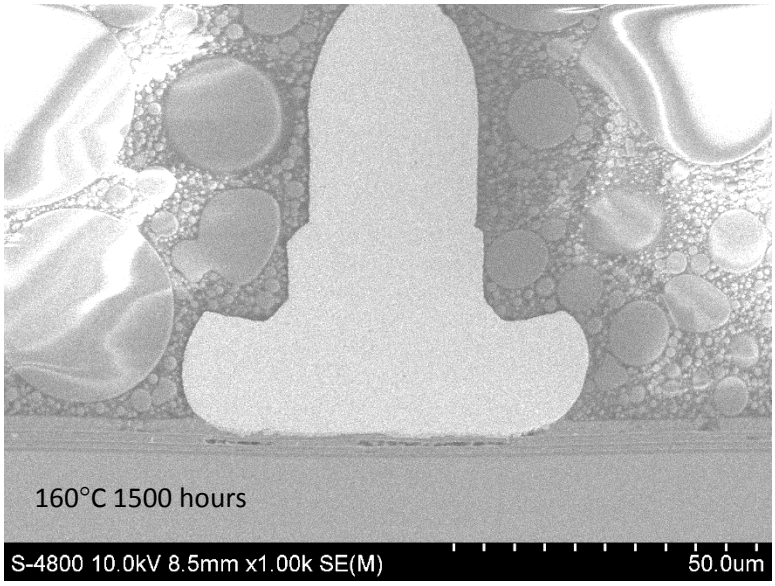

Figure 2: Cu wire - Al bond pad wire bond, FE-SEM cross section. UTA MMRL via CCMB

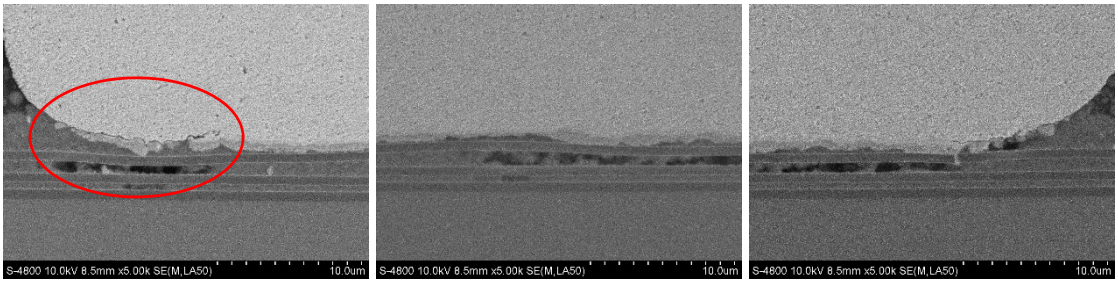

Figure 3: Cu-Al Wire bond interface. FE-SEM (SEI+BEI). UTA MMRL via CCMB

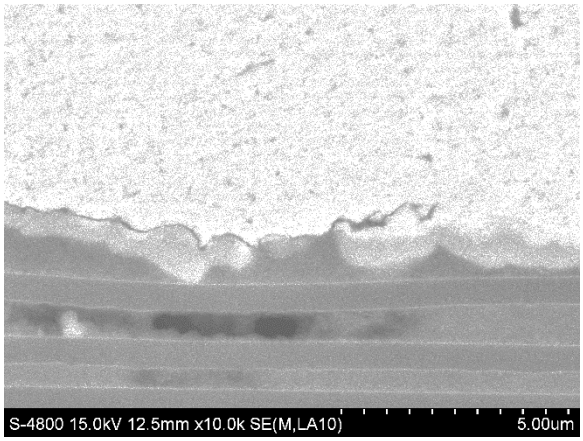

Figure 4: Cu-Al Wire bond interface crack. FE-SEM (SEI+BEI). UTA MMRL via CCMB

Table 1: Thin-film / Thin-film configuration used in sequence and formation energy studies[29].

Cu/Al thickness ratio	Atomic percentage Cu	Sequence of phase formation	End phases at 400°C	Stable phases at 400°C from the phase diagram
0.29	29	$Al_2Cu \backslash Al_4Cu_9$	$Al_2Cu + Al$	$Al_2Cu + Al$
0.56	44	$Al_2Cu \backslash Al_4Cu_9 \backslash AlCu$	$Al_2Cu + AlCu$	$Al_2Cu + AlCu$
0.71	50	$Al_2Cu \backslash Al_4Cu_9 \backslash AlCu$	$AlCu$	$AlCu$
0.87	55	$Al_2Cu \backslash Al_4Cu_9 \backslash AlCu \backslash Al_3Cu_4$	$AlCu + Al_3Cu_4$	$AlCu + Al_3Cu_4$
1.07	60	$Al_2Cu \backslash Al_4Cu_9 \backslash AlCu \backslash Al_3Cu_4$	Al_2Cu_3	Al_2Cu_3
1.26	64	$Al_2Cu \backslash Al_4Cu_9 \backslash AlCu \backslash Al_4Cu_9$	Al_4Cu_9	$Al_2Cu_3 + Al_4Cu_9$
1.58	69	Al_2Cu / Al_4Cu_9	Al_4Cu_9	Al_4Cu_9
2.38	77	Al_2Cu / Al_4Cu_9	$Al_4Cu_9 + (Cu)$	$Al_4Cu_9 + (Cu)$

Table 2: Formation energy findings by various studies referenced[29].

	E_a (eV)	reff
Cu (self)	1.425	[19]
Al (self)	1.02	[19]
θ-CuAl2	1.15	[29]
	0.78	[34]
	1.08	[31]
	0.87	[41]
	1.01	[40]
	1.02	[32]
	1.31	[37]
	1.31	[36]
η-CuAl	1.38	[31]
	0.93	[41]
γ-Cu9Al4	1.3	[29]
	0.83	[34]
	0.84	[41]
	1.21	[40]

1.1.2 Copper Aluminum Equilibrium Phase Diagram

Table 1 provides the quantitative details of the constituent elements in the Cu-Al system.

Table 3: Constituent elemental properties

	Atomic #	Atomic Mass	Atomic Radius - pm	Crystal structure	Lattice constant -a	Density -g/cm^3	electronegativity	Vol. Expansion -	resistivity -E-08	Group	Period	Valence	reference
Aluminum	13	26.98	144	FCC	3.61Å	2.7	1.61	69	2.6	13	3	3	[2]
Copper	29	63.55	128	FCC	4.05Å	8.96	1.9	51	1.7	11	4	2	[3]

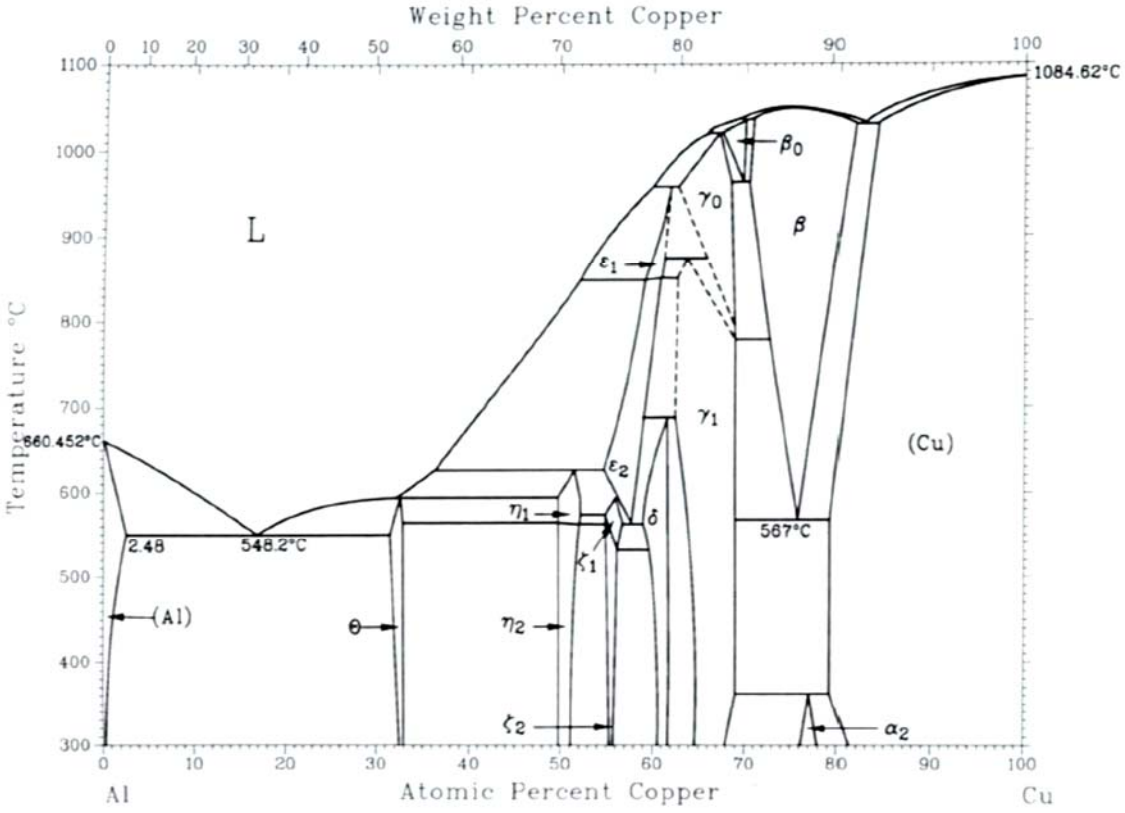

Figure 5: Cu-Al Phase diagram[4].

A phase diagram, or sometimes called the equilibrium diagram, is the roadmap for any study in intermetallic compounds (described later). Figure 5 shows a version of the Cu-Al binary

phase diagram produced in 1985[2]. Lines in the phase diagram indicate a boundary between two phases. A phase can be stable, metastable or unstable.

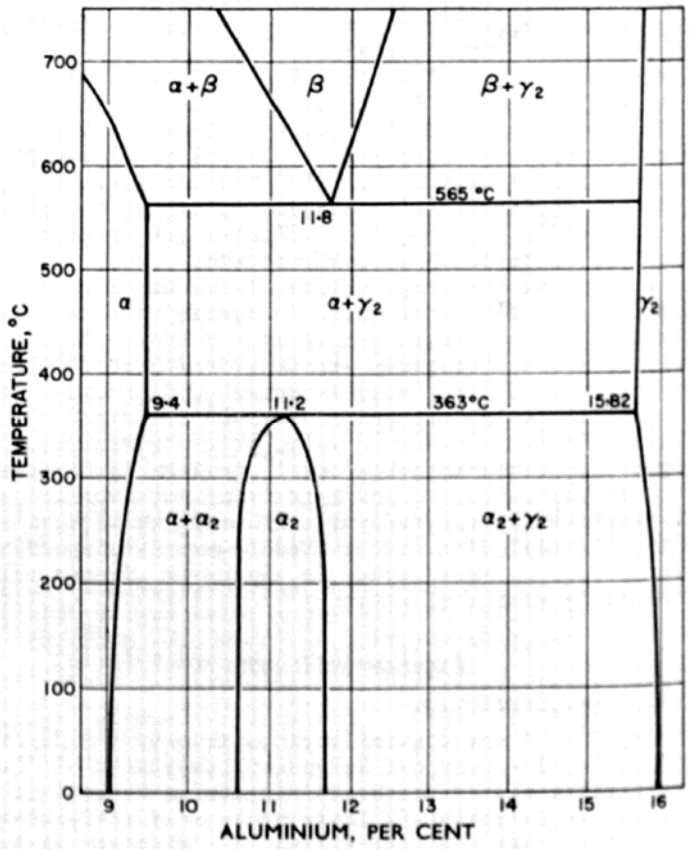

Figure 6: Revised Cu-Al Phase Diagram 9-19 wt. % Al6

Figure 6 is provided because we have an interest in the temperature ranges around 200ºC at high concentrations of copper. This work by R.P Jewett and D.J. Mack[6] helped to flush out details of the α_2 phase. It is called the revised diagram because phase diagrams for the Cu-Al system up till this date in 1963 were ambiguous in this region with a few referring to a phase *X* where α_2 is presented. The α_2, or *X* phase, had been investigated on several occasions previous to their work, including structural investigations that determined the FCC unit cell and lattice parameter[7] but it was Jewett and Mack that pulled the information together and submitted for calling it α_2. Experimental structure evaluations in 1933 by Subramanian et. al.[8], compelled

Massalski to describe the α_2 phase as "The close-packed Cu-rich phases have long-period superlattice structures that are constructed from two structural elements- the stacking of the close-packed layers without regard to ordering and the introduction of antiphase boundaries in the ordering sequence."[8]

Table 2 provides the quantitative* details of the intermediate phases found in the phase diagram.

Table 4: IMC Physical Data

	Designation	Crystal Structure	Lattice Constant(s)	Density	Composition	reference
$CuAl_2$	θ	BCT	6.06Å/4.87Å	4.27	33 at.% Cu	[5], [9]
CuAl	η	Ortho	6.95Å/4.16Å	5.31	50 at% Cu	[5],[9]
Cu_3Al_4	ξ	Rhomb γ-brass	(7.07 / 4.08 / 10.02)Å	~6.86	~55 at.% Cu	[5]
Cu_4Al_3	δ	Ortho γ-brass	n/a	n/a	~60 at. % Cu	[5]
	ϵ	γ-brass variant	n/a	n/a	~55-60 at. % Cu	[5]
Cu_9Al_4	γ	γ-brass	8.704Å	6.86	69 at. % Cu	[5], [9]
$Cu_{\sim 10}Al_{\sim 1}$	β	BCC	2.95Å	6.86	~70-80 at. % Cu	[5]
$Cu_{\sim 10}Al_{\sim 1}$	α_2	FCC	(3.65-3.68)Å	~7.25 -7.43	~88-91 at. % Cu	[6]

1.1.3 Hume-Rothery Phases / Line compounds

William Hume-Rothery was one of the pioneering forefathers in alloys. His work in developing predictive theories of solubility between constituent metals led to the development of the four rules titled for his work; the Hume-Rothery rules of solubility. These rules have been

very successful in predicting the solubility of systems prior to experimentation. Albeit there are systems that have been found where some other phenomenon has trumped these rules, they are for the most part solid guidelines. They are as follows:

Hume-Rothery rules of solubility

1. The size of constituent atoms must be less than 15% difference for solubility.

   $$\text{Difference} = \left(\frac{r_{solute} - r_{solvent}}{r_{solvent}}\right) * 100 \ \leq 15\%,$$

   where $r_{solvent}$ and r_{solute} are the atomic radii of the solvent and solute atoms.
2. As the difference between electronegativity between constituents approaches zero, solubility increases. The closer the electronegativity the greater the solvency, the more different the electronegativity the greater tendency to form IMC.
3. As the ratio of valence electrons, or the average number of valence electrons increases, so then does solubility. e/a is the common reference, where e is the number of valence electrons and a is the number of atoms in the composition.
4. The more similar the crystal structure between constituents, the greater the solubility.

Within a binary system, once rules 1 & 2 are established, only 3 & 4 can vary within the system. The metallic solid is described as metal ions within a sea of electrons. This is unlike an ionic bond system that has strong forces stripping the electron from one atom, or the covalent bond where forces draw the electrons into a shared configuration. The metal atoms seem to contribute electrons to the surrounding sea of electrons, allowing them to become ever so slightly positive to the surrounding "fluid" of electrons. Hume-Rothery was the one to pull together several researchers work and identify that within an alloy, some metals tended to contribute more to the "fluid" than others. That being the case, the outer most valence shell was considered as the contributing electron. Therefore, depending on the concentration at a given point, the short

range order within an alloy had a varying degree of "fluid" for the ions to move around in. Applying rules 1 & 2, if the size of the atoms permitted, the difference in electronegativity would allow for the metal atoms to reach a lower energy state by configuring into patterns forming a repeating order that becomes an IMC phase. If the e/a ratio (valence electrons contributed by each short range constituent divided by the total number atoms) was too much, the "fluid" between ions would be too thick for the weak electronegativity to attract into a uniform configuration. If this e/a ratio was too low, the ions would become more immobilized by a lack of "fluid" viscosity. The ideal range of Valence Electron Concentration (VEC) was 1.4-1.8. Each phase on a phase diagram marked with a Greek letter is an ideal range for IMC formations to occur and are therefore called Hume-Rothery phases. Hume-Rothery's work pertained to several binary systems where the γ-brass structure existed. Cu_9Al_4 was one such γ-brass structure involved in his research. The metal commonly referred to as brass is an alloy that can be composed of various constituents, although the main composition is accepted as Copper and Zinc (Cu_5Zn_8) which was the comparative companion in Hume-Rothery's work. Copper has 1 valence electron, Zinc has 2 and Aluminum has 3. Therefore:

$$\frac{e}{a}(Cu_5Zn_8) = \frac{[5x1]+[8x2]}{13} = \frac{21}{13} = 1.61;$$

$$\frac{e}{a}(Cu_9Al_4) = \frac{[9x1]+[4x3]}{13} = \frac{21}{13} = 1.61,$$

where e is the number of electrons and a is the number of atoms creating a ratio of electrons per atom.

Hume-Rothery determined that at this ratio, the alloy was least like a solid solution and most like a compound. The intermetallic compound or Hume-Rothery Phases[10].

1.1.4 Diffusion and Interdiffusion

Diffusion is mass transport induced by a potential accounting for storing of energy when a component is added. The sum of the various potentials affecting this component determine the conjugate driving force that provides the direction of movement. This is referred to as the diffusion potential and is dynamically referred to as flux. The foundation mathematics for diffusion were worked out by Fick[11]. Atoms tend to move from areas of higher concentration to areas of lower concentration until homogeny of the system is obtained. This is accounted for in the negative sign present in Fick's first law:

$$J = -D\frac{\partial \mathrm{C}}{\partial x}$$

where;

J is the notation for flux with units $\left(\frac{mol}{m^2 * s}\right)$;

D is the diffusion coefficient, sometimes called diffusivity having units of $\left(\frac{m^2}{s}\right)$;

C is the concentration or amount of component per unit volume, therefore units $\left(\frac{mol}{m^3}\right)$;

x is the distance with units of (m).

As the solution becomes more homogenous, the difference of concentration with respect to distance becomes zero and therefore movement of atoms goes to zero. This landmark equation gave the amount of change at any instantaneous moment, but did not provide the ability to determine the amount of time a diffusion process would take; the rate. For this, one equates the change in concentration with respect to time to the change in flux with respect to positon:

$$\left[\frac{\partial C}{\partial t} = -\frac{\partial J}{\partial x}\right] \rightarrow \left[\frac{\partial C}{\partial t} = -\frac{\partial}{\partial x}\left(-D\frac{\partial \mathrm{C}}{\partial x}\right)\right] \rightarrow \left[\frac{\partial C}{\partial t} = D\frac{\partial \mathrm{C}}{\partial x^2}\right]$$

In our case, the concentration at a given point can be described as how many atoms of constituent A and how many of constituent B per unit area. Fick's laws help us to determine the

potential for movement and the rate, but first we need the diffusion coefficient D for our particular system. There are a number of potentials that can impact diffusion. Previous literature treatments of this particular situation have attempted to establish thermal diffusion as the dominant driving force in order to establish rates and interactions[23, 29-44]. For our case, the identified potentials for atomic movement are:

Jump frequency establishes a basis for substitutional diffusion in a system where the constituent atoms are near enough in size that interstitial movement is unfavorable. Therefore, movement, or flux, is mitigated by the availability and movement of vacancies within the system. This is described through a local reference frame that will be called the crystal frame[19], or C-frame. The planes within the crystal provide a line for which to measure the passage of component A, B & V, where V represents the vacancies that must move in order for an atom of either component to move. This is mathematically described in the expression:

$$\overrightarrow{J_A^C} + \overrightarrow{J_B^C} + \overrightarrow{J_V^C} = 0,$$

where J represents the flux of each component and C is the concentration, A & B are the constituent elements and V is the vacancies.

Equating the flux of each component to zero indicates that if nothing is moving, then there is no change at the C-frame. Any movement across the C-frame will show that for one or more components moving in one direction requires the other component(s) to move in the other direction. This is based on an isothermal conditions where the vacancies are assumed to be in equilibrium with the system.

The diffusivity, or diffusion coefficient, *D*, is a factor that includes many constants for a system that is isothermal with an average number of vacancies per unit volume, in a periodic

structural configuration and a probabilistic factor for a jump at any given moment in time. For our system, Cu and Al is generally expressed as:

$$D_A = D_0 e^{\frac{-Q_{SD}}{RT}},$$

where

$$D_0 = \frac{1}{6}\alpha^2 z \upsilon e^{\frac{\Delta S_m + \Delta S_V}{R}}$$

where

α represents the distance that the atom will jump between the planes;

z represents the number of atomic locations that an atom could jump to;

υ is the temperature independent frequency that the atoms are vibrating at;

ΔS_m is the change in entropy of migration;

ΔS_V is the change in entropy of vacancies;

R is the gas constant for dealing with molar volumes;

$$Q_{SD} = \Delta H_m + \Delta H_V,$$

where Q_{SD} is the activation enthalpy for substitutional diffusion containing the summed values for atom and vacancy migration, ΔH_m is the change in enthalpy due to atomic migrations and ΔH_V is the change in enthalpy due to vacancy migration.

Described herein so far is the general observations of diffusion. The driving forces behind this transformation are varied. Each has roots in energy that is quantified under the category, Gibbs free energy. Energy is stored within a thermodynamic system. Nature drives all things to seek a lower energy level. As such, configurational energy is the first type of energy that can be reduced in a system. Through reconfiguration of the atoms within a volume, the system can obtain a lower energy. This is referred to as volume free energy ΔG_v. There is surface free energy ΔG_s, which is the energy of reducing surface area. μ_A is referred to as the

chemical potential and is the partial molar free energy associated with the change in molar composition. It is this value that bears the weight of various factors that modify the potential of a given system. For example; in the above description of substitutional jump frequencies, two components were considered. The atom and the vacancy. Based on their molar concentrations, diffusion increases or decreases. Even though vacancies are a null unit in terms of all aspects that can be used to describe an atom, they still have volume and mass to contribute to the systems overall free energy of volume. Using the notation outlined by Balluffi[19], $\Phi_i = \mu_i + \mu_V$. Where Φ_i is the flux of component *i* and *v* is for vacancies.

There are a number of potentials that have been excluded from our system, but in the interest of expressing them in order to show they have been considered, they are: Electronegativity of the different atoms in the alloy can respond differently to an electric field applied across the sample. This is Electromigration ($\Phi_i = \mu_i + q_i\phi$, where q is charge and ϕ is the field.)[19]. The response of hydrostatic pressure, P, on the system ($\Phi_i = \mu_i + \Omega_i P$, where Ω is atomic volume) [19]. The shape of the boundary between two diffusing metals can have a geometric shape conducive to promoting diffusion one way or the other. This is capillary motion ($\Phi_i = \mu_i + \gamma\kappa\Omega_i$, where γ is the surface energy and κ is the radius of the curve.). Or in the case of a faceted surface ($\Phi_i = \mu_i + \kappa_\gamma\Omega_i$) [19].

Of the potentials that cannot be excluded from our system. Applied stress along a boundary ($\Phi_i = \mu_i + \sigma_{nn}\Omega_i$, where σ is the stress and n is an x, y or z coordinate) [19]. The change in energy associated with a dislocations interaction with configurational change ($\Phi_i = \mu_i + \Omega_i \left\{\frac{[(\vec{b}^T * \sigma) x \hat{\zeta}] * (\hat{\zeta} x \vec{b})}{[(\hat{\zeta} x \vec{b}) x \hat{\zeta}] * \vec{b}}\right\}$, where $\vec{b}$ is the burgers vector and $\hat{\zeta}$ is the unit tangent) [19].

With those details in place, the macroscopic diffusion zone has a few qualities that bear attention as well. Most significant is from the displacement of vacancies in tracking the flux of

two components in a local reference frame. Smigelskas and Kirkendall developed their analysis of what is now known as the Kirkendall effect from this model. By tracking the movement of the vacancies, one can determine the conjugate sum of two elements interdiffusing with each other. One element will diffuse into the other at a faster rate than the opposite creating a "net" diffusion. The Kirkendall effect is generally observed and described by the voids that appear when the material becomes supersaturated with vacancies and they begin to merge. However, the Kirkendall effect simply describe the mass displacement due to the motion of vacancies.

L. S. Darken later utilized the results of the Kirkendall effect to develop the mathematics that describe the chemical diffusion coefficient for a binary system. The general equation is:

$$\widetilde{D} = (X_A D_B + X_B D_A),$$

where the X values represent the molar concentration of the subscripted constituent and D represents the diffusivity of the subscripted constituent.

1.1.5 Atomic Packing Factor and Volume Densities

The atomic packing factor is a term used to describe the amount of used / unused space in a periodic unit cell. The unit cell being the smallest unit of periodicity used to describe the whole. The lattice will have a coordinate intersection associated with one position in the unit cell. The packing factor refers to the amount of volume within the unit cell that is occupied by atoms. Atoms are spherical in shape, and unit cells tend to be cubic or reasonably cubic in nature. Therefore, there will be some space within a unit cell that is unused.

1.2 Mechanical Behaviors

1.2.1 Plastic and Elastic Stress / Strain relationship

Stress and strain are quotients used to describe the strength of a material. Stress units are generally force per unit area, and strain would be the change in length per unit length. The

strength of the material is an equilibrium between internal and external forces. As an external force is applied to a body, the internal forces resist a change in shape. As the magnitude of stress increases, the material will have no choice but to distort in shape as internal forces are finite. This description applies to homogenous and isotropic materials. The stress will translate through a plane of the material that begin to shorten (or lengthen depending on the direction of stress). This change in the length, per unit length is the material being strained. When the stress is removed, the internal forces of the material will attempt to return to their former positions. A full recovery to their previous unstressed position is a full elastic recovery. Perhaps though, there were bonds between atoms broken during the stressing of the material. The broken bonds cannot return to their prior unstressed position. Some small portion of the material will then remain displaced from the original position. If enough internal changes occur that the recovery of position is greater than 0.2% then it is referred to as plastic recovery. Within the 0.2% is referred to as the elastic limit.

With respect to stress, there are two types. Compressive stress is a load applied in such a way that the strain, or change in length per unit length, will become shortened. Tensile stress is the opposite, where the strain would be lengthened upon dimensional measurement.

1.2.2 Hardness, Dislocations

Having defined that applying stress will produce strain, the concept can be applied to the lattice. When the elastic limit of the metal is exceeded, atomic bonds will be broken that allow sliding to occur within the lattice, distorting the shape of the object. Sliding occurs preferentially where the amount of energy to break a bond is least. This occurs on the planes that are parallel to the direction of the applied force first. It is along these planes that plastic deformation begins to occur. As the stress increases, other planes with low angles to the direction of stress vector

begin to move. The movement of these planes not parallel to the direction of applied stress creates mismatches in the internal lattice. These mismatches generally form a line that are referred to as *dislocations.* It has a ripple effect commonly associated with the ripple created in a carpet being moved along a floor. A section of atoms in the direction of the shear become unattached and compress against perpendicular planes within the lattice. This creates a shortening of the measurement in the direction of the shear vector creating a change in the strain measurement. Figure 7 presents the diagram for a lattice that has seven vertical planes on top and bottom separated by a slip plane. On the top half, the planes have been compressed with a dislocation at the center. At positions a, b and c you will notice a vacancy in the lattice. Through substitutional jump, if these vacancies move to positions d, e & f, then the dislocation can climb, moving the slip plane up in the lattice. If these vacancies move to positions g, h & I.

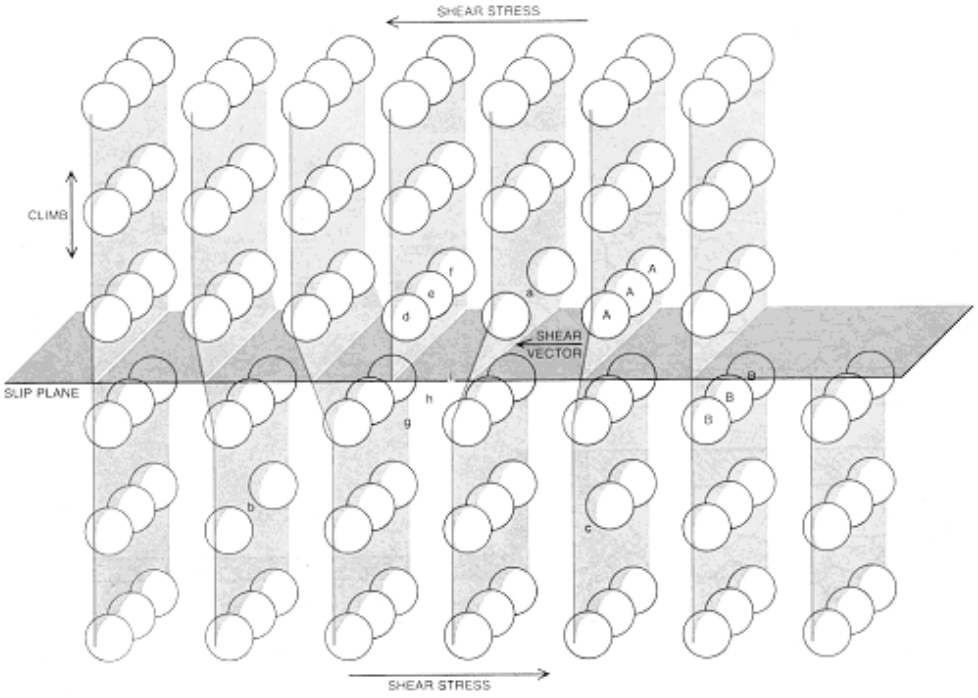

Figure 7: dislocation compression for an edge dislocation[17].

the dislocation moves down in the lattice, still called a climb. If the vacancies agglomerate at A, A & A then the strain held in the lattice can be relaxed by one perpendicular atomic plane along the shear plane. Repetitive movement to B, B & B will move the dislocation towards the edge where it and the vacancies can be annihilated.

Once dislocations form, sliding across a dislocation line at other angles becomes increasingly higher in energy as the angle between the dislocation and the intersecting sliding plane increases. This often forms an intersection between two dislocations where both dislocations become pinned at the connection. These situations are defined as kinks and eventually tangles. While a dislocation is unpinned, it can continue to move along directions perpendicular to its axis. Once it becomes pinned, the coordinate of the intersection has two axes with no common perpendicular direction that it can travel. These become the highest energy movements within the matrix. As deformation stresses are repetitively applied, the number of dislocations within a cubic volume increases. This is *dislocation density*. As dislocation density increases, more and more dislocations will become interlocked into a network forming a dislocation cell. When a moving plane of atoms becomes compressed against a dislocation, attempting to overcome the energy needed to move it, and then becomes pinned behind the direction of movement by another dislocation; the stress energy becomes trapped in the form of compressive stress. As this energy exists in the form of displacement of the lattice, it is called *strain energy*. Even though no temperature has been applied during the deformation process, this strain energy takes the form of an *internal energy* and is therefore thermodynamic in nature.

The process that has been described here, with no applied temperature [(relative to the materials melting temperature (T_m)] is referred to as cold working. During the deformation process, approximately 90% of the stress energy applied will be transformed into heat caused by

frictional sliding of planes against each other. The remaining 10% will become stored in the metal as strain energy and surface energy. The surface energy is the un-bonded atoms along the interfaces of the dislocations and grains within the metal. As the strain energy is thermodynamic in nature, the amount of strain energy that a metal can hold (per cubic volume) is relative to the metal T_m.

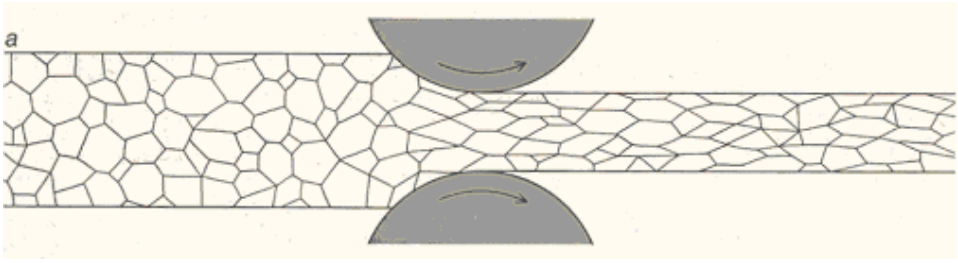

Figure 8: example of cold work deformation[13]

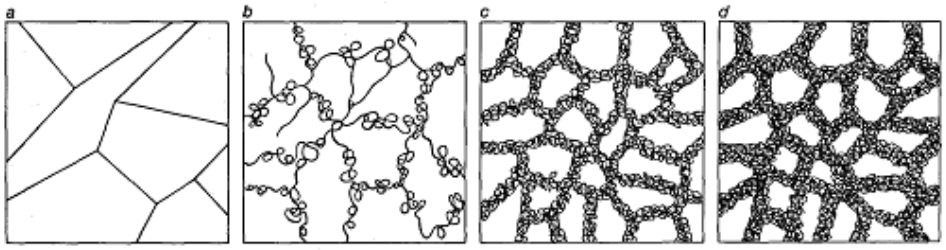

Figure 9: Cold work example showing a.) undeformed. b.) formation of dislocation tangles at boundaries. c) Formation of dislocation cells. d) Thickening of Cell walls[13].

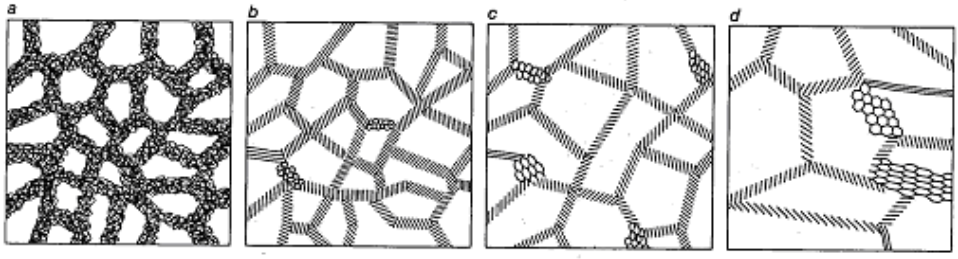

Figure 10: Annealing process showing a) prior to recovery. b) Dislocations annihilate thinning walls into misoriented boundaries. C) Recrystallization consumption of strained grains by non-strained grains. D) Restoration to near pre worked state[13].

The deformation process is rarely uniform through the metal. The dislocations within a metal are not thermodynamically stable. Physics demands a lower energy state, as such, the metal seeks a configuration that will achieve this lower energy. Given enough time, self-diffusion of the metal will reduce the internal energy to its original strain free state. This is known as *annealing*.

1.2.3 Interface Dynamics

It is important at this point to interject the concept of interface dynamics. We have described how stress, strain and diffusion occur in a lattice. However, what if the lattice is inconsistent? This occurs at an interface where atom sizes prevent the lattice parameter to be the same across an interface. This is known as *coherency*. The term coherent is applied to a lattice whose parameters are so close that every atom in the interface has a partner atom across the interface to form a bond with. This can only happen in a lattice where every atom is the same size and also has the same plane parallel across the interface. Therefore, the lattice must contain a homogenous collection of all the same atom and there must be a zero degree difference in the coordinate grain angle. Coherent interface do still exist between binary systems and are defined as a high degree of atomic connections across an interface.

The next term to be defined is *Semi-coherent*, which is an intermediate measure of atomic connections across an interface. And finally, the remaining definitions is incoherent, defining the case where few connections across the interface are maintained. An important note to bear in mind here is that homogeny is only a small factor in coherency. A similar homogeny along two different planes can create a semi- or incoherent interface due to a high angle of misorientation between the crystal orientations of two grains. Therefore Cu (111) to Cu (200) might me more incoherent than Cu (111) to γ_2 phase (330) which are closer together in interplannar distance than

Cu (111) and Cu (200). Coherency has to do with the geometry of atomic spacing in the orthogonal frame where interplannar distance is one dimensional.

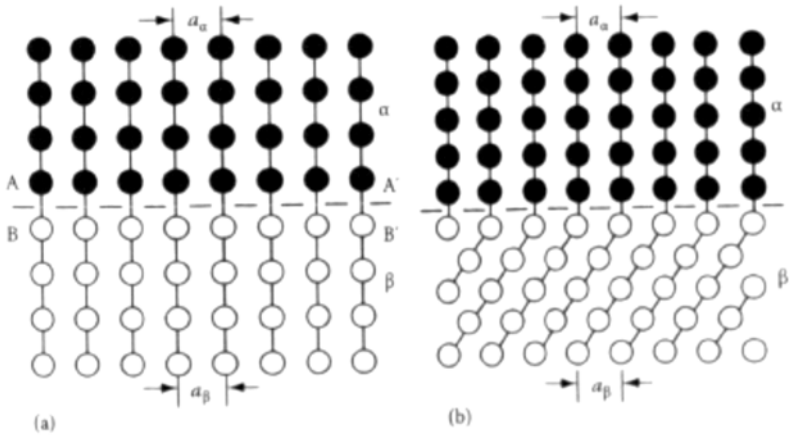

Figure 11: Strain free coherent interfaces. a) Each atom of β composition has an atom aligned across the interface. b) Even though the lattices are not aligned, the interface atoms have bond partners across the interface[17].

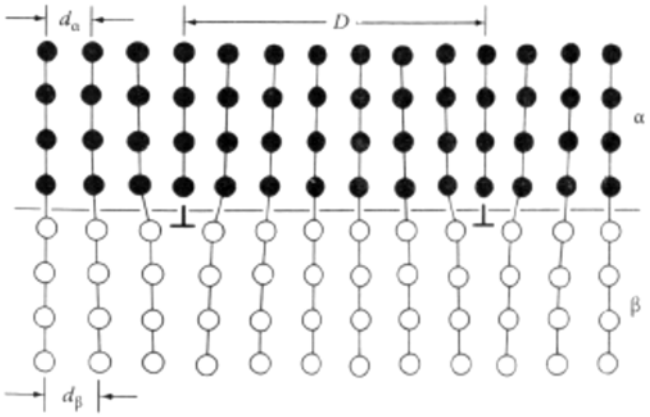

Figure 12: Semi-coherent interface where edge dislocations are necessary to maintain coherent bonding across the interface[17].

The last note concerning coherency and interface has to do with the transfer of elastic stress. Compressive or tensile stress requires atomic bonding, therefore coherency of an interface is important to how much stress can be conveyed across an interface. It is a linear

relation correspondent to the percentage of atoms at the interface that are atomically bonded. Therefore, an interface with high coherency will translate more stress than an incoherent interface. An incoherent interface will tend to slide along disconnected planes creating KIIc crack situations.

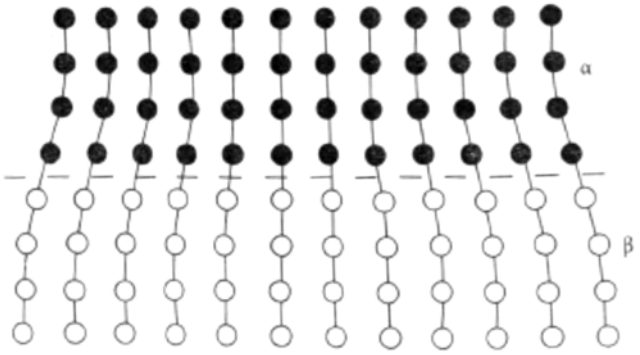

Figure 13: Without the edge dislocations shown in Figure 11, the β lattice becomes compressed at the interface and α becomes tensile stretched with lattice stress[17].

The next interface to be considered is the interface between two grains within the same solid. A grain is defined as a volume of material whose lattice has a regular repeating periodicity. The boundary of one grain within the solid will be adjacent to another section of lattice whose coordinates will be determined by the life of that grain and can have any of its three coordinate axis turned along a 180º range for extremely different lattices. In cubic lattices these dissimilarities are minimized due to isometry in orthogonal directions. By their nature, grain boundaries are typically incoherent and stress is generally only transferred when it is compressive in nature and only in a direction normal to the surfaces of the grain that are parallel to the direction of stress.

The primary significance of grain boundaries for this work has to do contribution to the phenomenon of diffusion. As described earlier, diffusion in the Cu-Al system occurs by substitutional vacancy jump mechanics. Due to incoherency of grain interfaces, grain boundaries contain a higher concentration of vacancies than the bulk material. As a result, diffusion along grain boundaries, referred to a pipe diffusion, occurs at a faster rate due to the proportional availability of vacancies. This volume of vacancies varies on the amount of angle difference between two grains across an interface. Figure 14 shows three different grain boundary angle differences at the interface. One important aside of figure 14 is the abundant source of vacancies present in a high angle grain boundary as opposed to a small angle boundary.

In FCC materials with a high Stacking Fault Energy (SFE), another type of grain boundary can form called a twin boundary. In a twin boundary, the interface between the two grains aligns favorably to form connections that place atoms in a position that is a reflection of

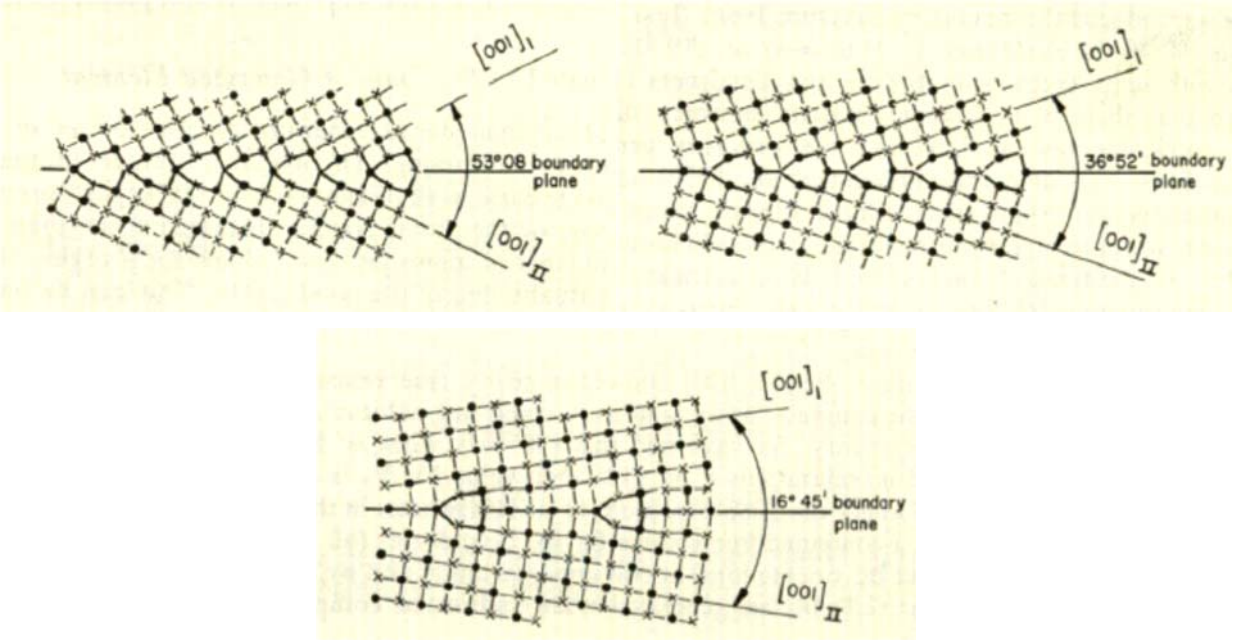

Figure 14: 3 different grain boundary interfaces in decreasing angle showing the amount of volume present based on grain angle difference[18].

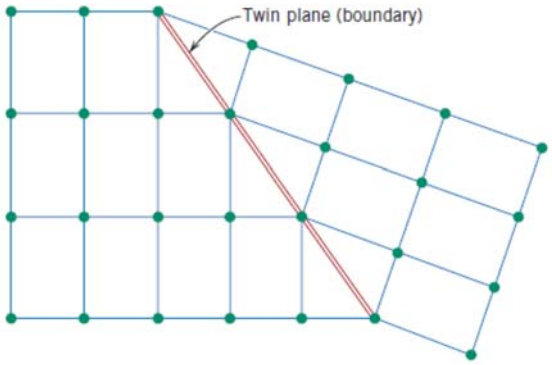

Figure 15: Twin grain boundary. Red lines show the reflection plane[19].

the atoms across the interface. The grain boundary becomes the reflection plane. Twin grain boundaries have fewer vacancies contained within, but are still higher in bulk free volume energy than a single grain lattice. In copper, twin boundaries have been found to be thermodynamically unstable[18].

1.2.4 Work hardening / Annealing

Annealing allows the opportunity to control the work hardening process by increasing the temperature and halting it at the desired state. By applying temperature, the average dislocation density across the material can be equalized and lowered as needed. Brittle areas with the highest strain energy will disperse their energy first, equalizing across the system. The annealing phenomena consists of three processes.

Recovery – As the temperature increases, the energy needed for a plane to slide decreases. Dislocations with high strain energy pinned within low angle situations finally have enough energy to overcome their situation and move to positions of lower energy. It is during recovery that areas of higher and lower dislocation density equalize. Dislocations with opposite polarity are attracted to each other and annihilate. Point defects in the lattice will also have enough energy to move to lower energy locations at dislocations and grain boundaries. During

recovery, the conductivity of the metal will increase, the amount of lattice strain will decrease and the number of point defects within the system will decrease[15].

Recrystallization – Temperature is more of a driving factor for annealing than time is. "Doubling the annealing time is approximately equivalent to increasing the annealing temperature 10ºC." –Deiter[15]. As temperature + time increases, dislocations continue to move to lower energy locations. During this dislocation movement, when dislocations opposite in their structure come in contact, they cancel each other out; restoring order to the lattice. Fewer dislocations in the lattice is lower in energy. This is known as *dislocation annihilation.* As dislocations density decreases, areas of strain free lattice form becoming the nucleus for the third stage grain growth. Atoms within strained grains surrounding the new strain free grain will begin to diffuse across the grain boundary to join the stress free grain. Macroscopically, this appears as grain growth into these nearby high strain content grains. For many metals, dislocations will form into tangles due to interaction slip plane pinning, strain free lattice forms preferentially in areas away from these tangles creating the geometry of cells of strain free lattice contained within walls composed of dislocation tangles. This is typical of metals with low stacking fault energy. Cu has an intermediate stacking fault energy, and falls into the region of metals whose dislocations tend to agglomerate into a crowding regions. This crowded region forms misorientations between sub-grains but doesn't form the dense dislocation walls present in lower stacking fault metals. Dislocations in dislocation wall cells in lower stacking fault energy metals tend to hold more strain energy than metals like copper. The crowding configuration allows dislocations to continue to annihilate where the wall structure tends to trap the dislocations from moving and annihilating. The result is a microstructure with a lower

dislocation density, a more spherical grain structure, and lower internal strain than other metals whose physiology prevents these microstructural advantages[15].

Grain growth – as temperature + time increases and dislocation density decreases, lowering internal energy further and further; surface energy, which had been two low in magnitude before, becomes the next physical change for the system to reach a lower state of energy. The strain free lattice, nucleated by recrystallization, becomes the growth platform for lower energy grains. Stress free lattice grains begin to grow into strained grains through a diffusional process where the atoms in the strained grain jump across the grain boundary to join the strain free lattice. As atoms join the strain free lattice, vacancies move the opposite direction into the strained lattice where their presence assists in the annihilation of dislocations[15].

Dynamic recovery and dynamic recrystallization. Up till now, we have discussed concepts as they apply to the static case. However, hot working of material has become of significant interest in the past half century. Hot working differs from the process described in that both deformation and temperature are applied simultaneously. Naturally one would think that this would combine aspects of both cold-work and annealing but the results are subtly different and they have been attributed to concepts known as dynamic recovery and dynamic recrystallization[13].

Simply put, dynamic refers to deforming material while it is at a temperature where recovery or recrystallization would occur if it were not being actively deformed. Metals with low stacking fault energies tend to experience dynamic recovery. During dynamic recovery, the elevated temperature reduces the energy needed to distort the lattice. As deformation occurs, the

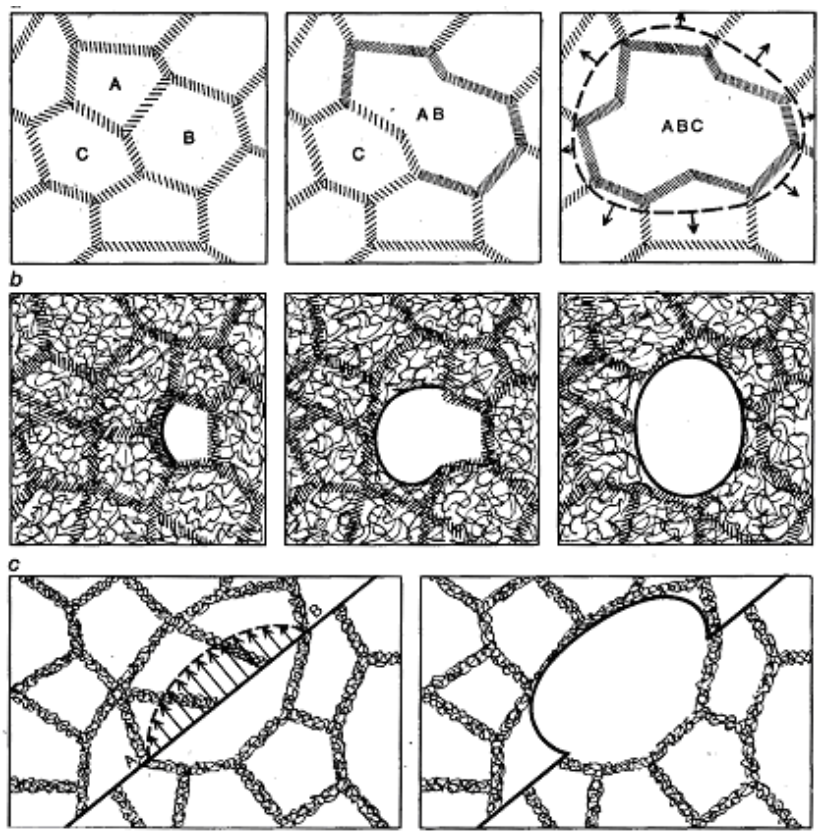

Figure 16: Nucleation of a recrystallized grain. Beginning just after recovery a) Dislocations in cells marked A and B attract one another to sub-boundaries, where some can annihilate. Those that do not annihilate form a misoriented sub boundary where atoms can diffuse across to the strain free grain until the boundary is pushed into a perimeter boundary. The sub-boundary between the new grain and grain C is less misoriented than other boundaries therefore the process repeats until grain C becomes a part of the new grain. The geometry of the final grain shape will promote dislocation mobility at points and bulges. b) This recrystallization example shows the area with little to no dislocations. Atomic and vacancy diffusion promotes the growth of the strain free region. d) Highlighted here are the boundaries pinned locations at A and B and from the first slide to the second shows how the strain free area bulges into the smaller higher strained grains to consume them[13].

grains are reduced in size by the breaking mechanism in cold working, but the internal lattice to each grain remains less strained than in cold working. This is achieved in an equilibrium aspect where dislocations are being generated by the deformation of the material but the temperature allows the dislocations to move and annihilate at a rate as well. The resulting internal strain of the metal will be determined by whether the dislocation formation was greater than the dynamic recovery annihilation of dislocations or vice versa[13].

Metals that experience dynamic recovery tend to experience normal recrystallization after deformation is complete. Metals with higher stacking fault energy, with sub grain boundaries, tend to experience dynamic recovery. These metals have dislocations that are already more mobile than metals with dislocation cells. With this, the metal experiences normal recovery prior to deformation. Once deformation begins, the sub grains can become new grains and the distortion of the lattice can allow the formation of strain free grains. Once again an equilibrium state is formed where some grains will be broken down by the agglomeration of dislocations annihilated while other portions of the lattice will be developing new grains. Balance and final state are achieved by the competition of strain free grain formation and stained grain consumption by recrystallization[13].

As a result of dynamic recrystallization, the average grain size across the material tends to be more spherical in shape than a cold worked then annealed sample.[13]

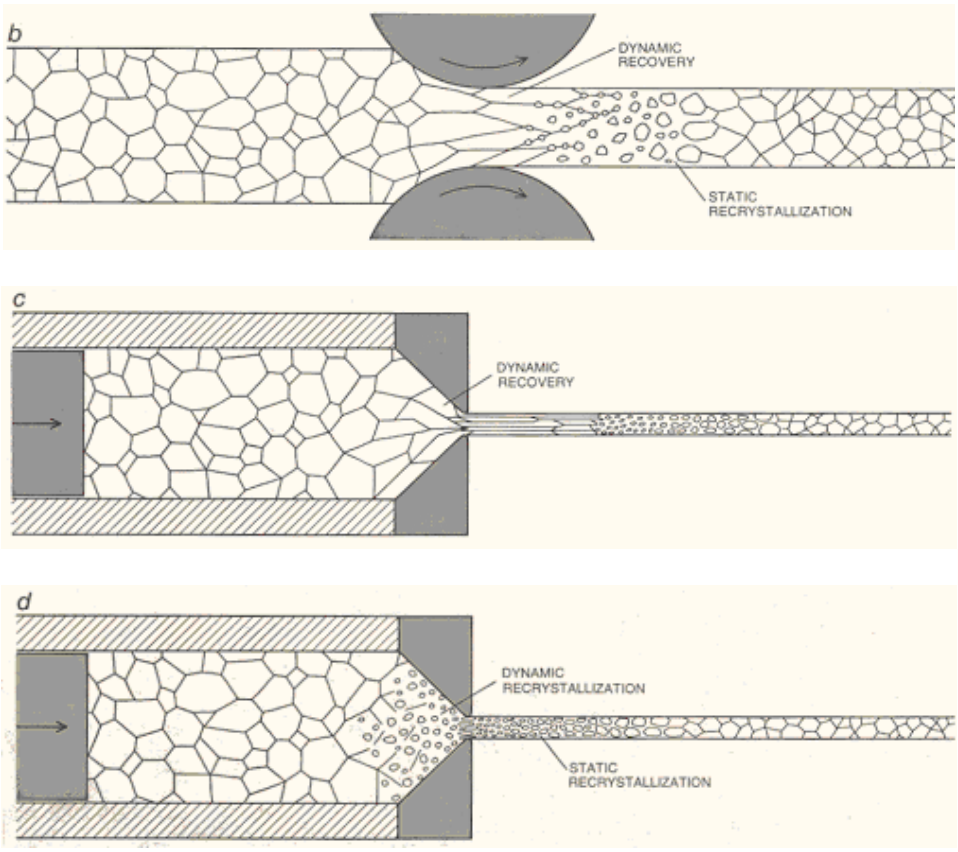

Figure 17: Examples of hot-working deformation of material. b.) Rolling of a low SFE metal. c) Extrusion of a low SFE metal d) extrusion of a high SFE metal[13]

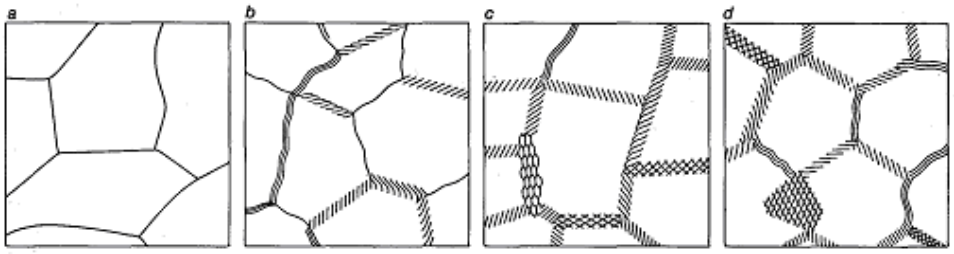

Figure 18: Example of Hot Working. a) Pre worked microstructure. b) After some deformation. c) Deformation continues, grain misorientation boundaries thicken. d) Finished state with grains more uniaxial and regular[13].

Chapter 2

Experimental Setup

2.1 Preparation of Cu-Al diffusion couple

2.1.1 Hot rolled half hard Copper (Cu)

As received material

- C11000 Half Hard Cu (ASTM 8.3 Hot-Rolled and hot-rolled and annealed plates of Copper UNS Nos. C11000 and C12200 shall have 40% minimum elongation in 2 in.)
- 99.94% Cu includes +Ag.
- ASTM B-152/B152M-13.
- Thickness 0.04 inch.
- Hardness RF 84, (77-89 Rockwall F scale)
- Tensile KSI 42.3 (32-46)
- Yield KSI 40.4
- Elongation % in 2" – 13
- Cond% IACS 100.4
- Resistivity should not exceed 0.15328 ohm*g/m^2 (ASTM ch13.1

2.1.2 Annealed Copper (Cu)

Portions of the as received material were submitted to heat treatment at 400ºC in order to relieve internal stress and promote grain growth. Figure 3 represents the cooling time for the annealed samples. According to literature[8], recrystallization in pure copper can begin at temperatures as low as 200ºC. Cross referencing this with ASTM standards, there is a fair amount of agreement that 400ºC is well within the range recrystallization and grain growth. Our sample was maintained at 400ºC for one hour and then allowed to cool down in the furnace. Multiple temperature readings were obtained to obtain the equation of cooling. The sample was removed from the furnace 12 hours after the heating cycle was shut off.

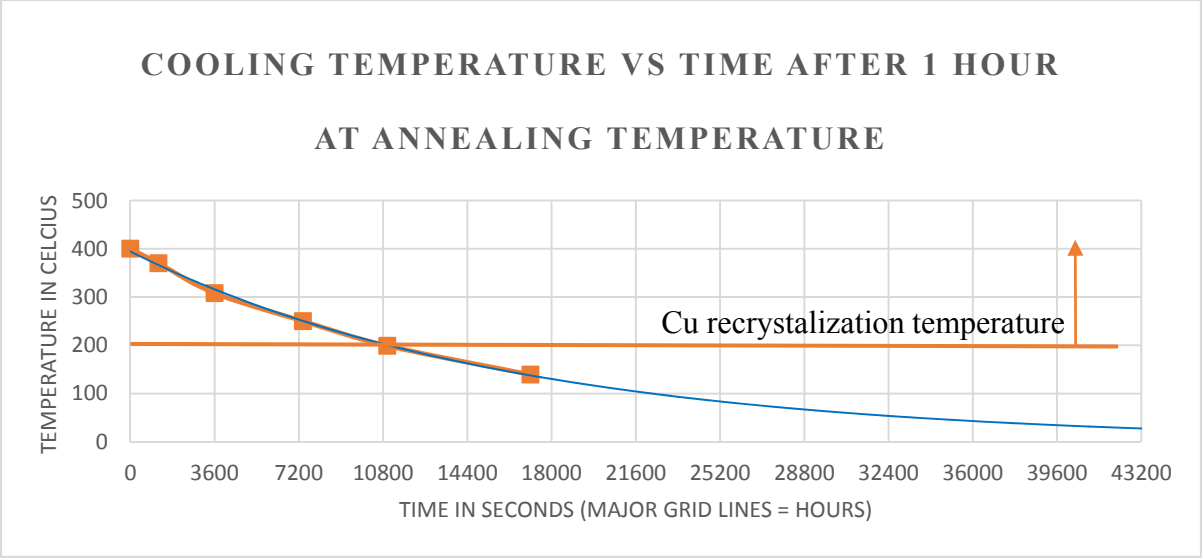

Figure 19: Graph showing annealing time and temperature

2.1.3 Surface preparation

One sample of the as received and one annealed sample were polished and lapped to 0.3 µm. White light interferometry was performed on the sample to obtain an average surface height variation. The polished samples were dispatched to be sputtered with aluminum using

2.1.4 Microstructure Analysis

Annealed sample was analyzed via chemical etchant with optical micrography and SEM-EBSD for microstructure analysis.

The annealed sample and the as received sample were microhardness tested to confirm that the material was in fact softened by the annealing process.

2.1.5 Sputtered Aluminum (Al) interface

Aluminum develops an oxide layer faster than most processes can circumvent. In order to minimize the amount of oxide present in the Cu-Al interface, the samples were dispatched to the Shimadzu Institute Nano Technology Research Center where Al was applied to the smooth surface via evaporative physical vapor deposition (PVD) using an AJA ATC Orion Series UHV

Sputtering System. The Ultra High Vacuum (UHV) prevented the aluminum from interacting with any oxygen to form the undesirable oxides. The depth was to be 3μm, onto the smooth surface of the two samples [as received half-hard (hard) and anneal softened (soft)]

2.1.6 Post sputtering handling

Sputtered samples were separated into smaller pieces measuring 1cm square. Due to the fact that a rolled sample has a rolling direction to its microstructure, a common mark was crimped into each sample to maintain uniformity in future testing.

2.2 Characterization Techniques

2.2.1 X-ray diffraction

X-Ray diffraction is one of the most well developed tools in the study of solid materials. Its origin dates back to the early 1900's although it did not obtain widespread use until the 1920-1930's. For many years it was the only easily accessible tools for the material scientist to use and as such, they discovered many ways of extracting data using it. Using X-ray diffraction, you can determine the crystalline structure of an unknown material, phases, material composition, grain size, grain orientation, and even stress between atoms. The term diffraction was coined by Francesco Maria Grimaldi in the mid 1600's from the Latin word diffringere, 'to break into pieces'. Grimaldi studied how light changed directions. Diffraction was used extensively throughout the 17^{th} and 18^{th} century for the study of light. In 1895 Henry Röntgen discovered x-rays. Following the discovery of x-rays came many practical applications for the use of this unknown radiation. It was 17 years later in 1912 that Max Von Laue experimentally proved that x-rays were in fact electromagnetic radiation like light, but whose wavelength is three orders of magnitude smaller. His method of proving this was using a solid material as a target to detect if x-rays diffracted as light does. Laue's focus was on the radiation and not the material, it was

later the same year that William Henry Bragg and his son took up on Laue's work and developed the working theory of crystal atomic structure.

The premise that allows this concept to work is the ratio in size of x-rays and the interatomic spacing. X-ray wavelength (λ) ranges from 0.5Å to 2.5Å. Interatomic spacing of the pure elements ranges from ~2Å to almost 6Å. The symbol Å, pronounced Angstrom, refers to the unit scale of measurement equivalent to $1x10^{-10}$ meters. By comparison, visible light is 4,000Å to 7,000Å, which upon incident to a solid material reflects off of or transmits through the material. Because of their size, x-rays can pass between or reflect off of atoms depending on the geometry of the incident.

The English physicist Sir William Henry Bragg (1862-1942), pioneered the determination of crystal structure by x-ray diffraction methods, for which he and his son William Lawrence Bragg received the 1915 Nobel Prize for physics. Using previous theories and hypothesis on the structure of materials on a very small scale, the Braggs conceived of an atomic crystal as an infinite series of planes of atoms, each reflecting some portion of the incident radiation. The observed reflected signal should attain a local maximum amplitude when the reflected waves interfere constructively.

Now consider two parallel rays reflecting off adjacent crystal planes. We assume that the usual law of reflection applies, so that the angle of incidence is equal to the angle of reflection. If this is the case and if adjacent planes are separated by a distance *d* and the rays reflect off adjacent crystal planes, then the additional distance traveled by the ray reflecting off the deeper plane is $2d \sin \theta$ (See Fig. 20). Constructive interference occurs when this path difference is equal to an integral number of wavelengths, so

$$2d \sin\theta = n\lambda ,$$

where *n* is an integer, λ is the wavelength of the incident electromagnetic ray and *d* is the interplanar distance.

Notice that this requires the wavelength λ < 2*d* if any constructive interference is to be observed. This is because the results from $\sin\theta$ range$\pm(0-1)$, if $2d < \lambda$, no meaningful result would be produced mathematically. What this means qualitatively is that the wavelength (λ) being used is too large to fit between lattice points of the crystal. If the crystal separation and source wavelength are known, then the brag equation can be used to predict the angle θ where constructive interference is expected.

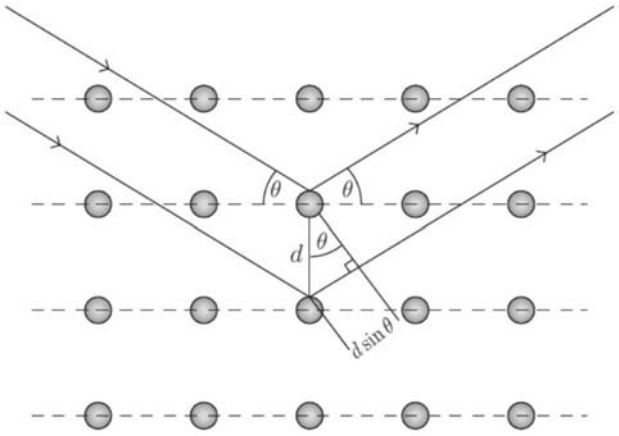

Figure 20: Bragg Diffraction conceptual diagram

Bragg's Law

We know from the study of light, that interference is based on the specific frequency of light because multiple wavelengths will diffract at different angles based on their wavelength. Similarly, if our x-ray source contains a variety of wavelengths we will receive multiple signals and our analysis will be compromised. If you single out, as close as possible, a particular x-ray wavelength, then the results will be cleaner for analysis. Rearranging Bragg's equation:

$$n\lambda = 2d\sin\theta_B \rightarrow \lambda = 2\frac{d}{n}\sin\theta_B\,,$$

To give meaning to the term $\frac{d}{n}$ let n represent the order of reflection. Meaning that the top layer of atoms of a solid would represent the 1st order, the 2nd layer beneath that would be 2nd order, etc. Meanwhile, in the Bravais lattice principle, the directions in a crystal that correspond to the xyz coordinate system are hkl. The distance between any two atoms within a lattice is:

$$d_{hkl} = \frac{a}{\sqrt{h^2+k^2+l^2}},$$

where a represents the lattice constant of a particular structures unit cell, and $\sqrt{h^2+k^2+l^2}$ is the Pythagorean theorem applied to the difference in distance in a cubic structure, or simply the order of reflection distance. This places Bragg's diffraction law in the form we need to use for structural analysis of the lattice.

$$\lambda_{x-ray} = 2d_{hkl}\sin\theta_B$$

Bragg's Circle (Θ-2Θ)

The diffractometer used for analyzing the material in this experiment is a Seimens D500. The D500 x-ray unit uses the configuration known as a Bragg's Circle, or Θ-2Θ. In order to find a particular diffraction angle you have to adjust the angle of the source, sample and detector. In this configuration the source will be stationary throughout the process and the sample and detector will move through an arc so that the surface (face) of the sample travels through the Θ-2Θ range designated for the experiment. The name Θ-2Θ, comes from the literal translation of the configuration. In order to detect a diffracted angle, the detector travels at a reciprocal angle thereby making the recorded angle twice the incident angle. The process of taking multiple readings at various angles will be referred to as the scan. As the D500 goes through its scan, most angles will collect only minor readings from scattered x-rays. The scattering of the amorphous structure will create many small peaks. Peak height is produced by the number of

counts that the detector records for a given angle. An amorphous structure has very few similar peaks, so the height of these peaks will be very small. The collective whole of these amorphous structure peaks creates what is called the background in the data. When a Bragg's angle is found that corresponds to a reflection plane in the lattice, the detector receives many counts from the number of atoms that are in that plane. Therefore the intensity of the peak will be higher than the surrounding background. Principle planes will collect more intensity than minor planes. Figure 5 shows the layout of Bragg Circle.

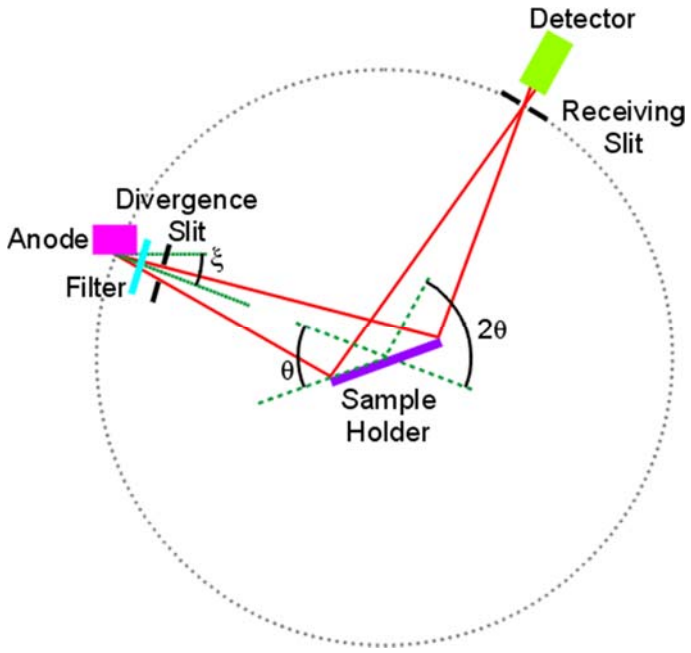

Figure 21: Bragg's Circle Configuration

The International Centre of Diffraction Data (ICDD), formerly known as the Joint Committee on Powder Diffraction Standards (JCPDS), maintains a comprehensive database of diffraction data for material analysis. Using their data you can compare your results and thereby identify metals, phases, minerals and many other structures. Having performed a variety of XRD scans on our samples, it was discovered that a majority of the activity in our experiment was happening in a 2θ range of 38º to 90º. Therefore, the standard full range scan presented in this

work will be 35º to 91º in order to focus on activity relevant to the work. Figure 6 presents diffraction data obtained from ICDD for the relevant structures that we expect to see in our system. There are a variety of other possibilities, such as Cu_2O, $CuAlO_2$, CuAl (η), β, $\varepsilon_{1\text{-}2}$, Cu_3Al_2 (δ_2), and Cu_4Al3 (ζ_2). ICDD contains diffraction data for Cu_2O, $CuAlO_2$, and CuAl (η) for which our data has been compared and found to be lacking in sufficient peak intensity to definitively characterize. To the extent of our search, we were unable to locate β, $\varepsilon_{1\text{-}2}$, δ_2, and ζ_2 structures in the ICDD database. The database is arranged by composition

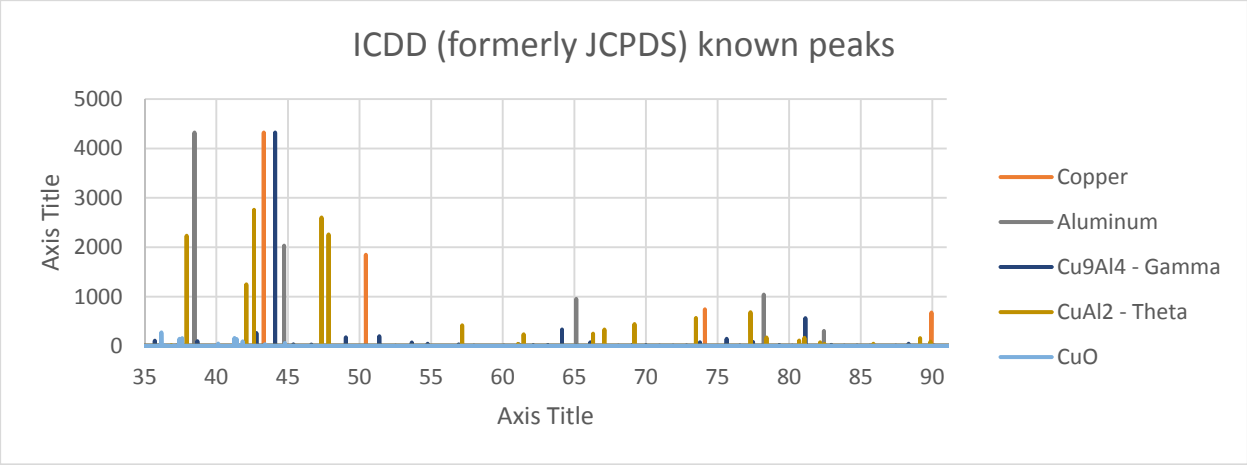

Figure 22: ICDD known peak data

2.2.2 Micro-Hardness test

The microhardness tester uses a tip made of diamond, shaped in the form of a 4 sided pyramid to create an indention in the surface of the material being tested. The amount of pressure is set by the operator. In our case, the pressure was set to 500 grams. The operator then measures the span across the indention from corner to corner of the 4 sided indention to determine how deep of an indention was made. Harder materials will have a smaller indention, softer materials will have a larger one. The machine is programed to calculate the hardness on the Vickers scale (HV). At a given location where an indention is made, the hardness can vary based on the microstructure in the vicinity around the tip. More accurate results can be obtained by statistical

averaging of many measurements. The results are however sufficient for an approximate range of hardness in our case.

2.2.3 SEM-EBSD Raw material

Among the tools for material characterization, the Scanning Electron Microscope (SEM) is quickly becoming one of the most commonly found in any lab. Its ease of use, versatility, operational expense, size, and cost per unit make it ideal for many labs. The most common use of the SEM is imaging at magnifications far beyond the limit of optical microscopes. However, with various attachments and analysis of responses not available in optical microscopes, the information that can be extracted from a sample make the SEM a frequent go to for characterization of materials. In our experiment we used a variety of functions; secondary electron imaging (SEI), backscattering electron imaging (BEI), Energy Dispersive X-ray (EDX) analysis and electron backscattered diffractions (EBSD).

An SEM is a device that produces free elections and accelerates them in a controlled line at the target. These electrons collide with the target and produce a variety of responses that can be analyzed into different results.

Before launching into electron interactions a description of the machine and how these interactions are orchestrated will lend insight. A SEM organizes and accelerates a steady “beam” of electrons in a column that can be directed to a designated point on the sample of a diameter as small as approximately 4 nanometers in diameter.

The basic components that make up the SEM are:

- Electron source: Commonly referred to as an electron gun. The two common types are thermionic and field emission.
- Vacuum chamber: Since electrons will interact with gas molecules in the air, a vacuum is necessary for proper function.
- Potential plates (Anode): between which a potential difference is applied to accelerate the electrons to desired energy levels.
- Collector and condenser lens: In spite of their name, the lenses in an SEM are not true lenses, as in a solid that transmits radiated wavelengths through, but electromagnetic devices that produce a magnetic field within a region that the negatively charged free electrons pass through in order to redirect their path as desired. Example at right. The collector lens is closest to the electron source and pulls electrons into the column that will focus them. The condenser lens columates and converges the beam of electrons to a desired formation.

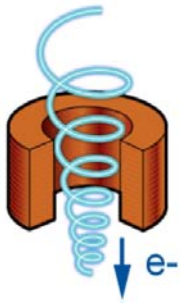

Figure 23: Condenser coil cutaway schematic

- Apertures: anywhere from one to many within the device to screen out divergent electrons that fail to redirect into the beam path.

- Scanning lenses: these lenses redirect the beam path on an x-y coordinate system with z being the normal to the sample surface. This allows the system to "point" the beam to designated coordinates across the desired scanning area. This is a pixilation of the sample so that collected intensities from each specific location can be redirected to a visible monitor at the same coordinates to produce the image of the surface.
- Objective lens: This is the lens closest to the sample. Receiving the converged beam from the condenser lens, the objective lens redirects the electrons into a cone that will place the apex, or point, of the cone on the sample with a desired "spot" size.

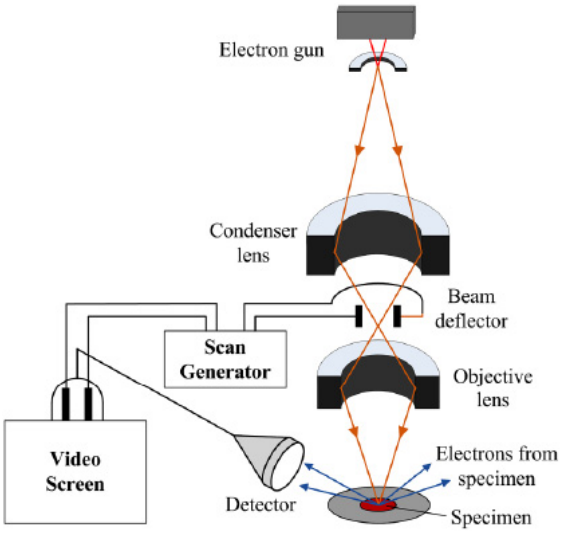

Figure 24: basic components of the SEM and their operational location within the device.

Numerous interactions can occur when the electrons reach the sample. Among these are when an incident electron collides with an atom in the sample. In one case, the electron collides with an electron in the sample atom transferring a portion of its momentum to the samples electron and rebounding at small angles relative to the incident direction. This is an inelastic collision and is the source of secondary electrons. In a second case, the electron passes through the sample atom having its direction changed by the electrostatic interaction with the electronic components of the atom. The angle of deflection is large relative to the incident direction. This

is considered an elastic collision and is the source of backscattered electrons. An elastic collision is defined as a collision where the energy is conserved at a macro-scale; in this case the incident electron deflects from its 'collision' with the sample atom, even though it did not 'collide' with anything inside the atom. As a result, the electron exits the interaction with a majority of the energy that it had prior to the interaction, justifying the definition of the elastic collision. The

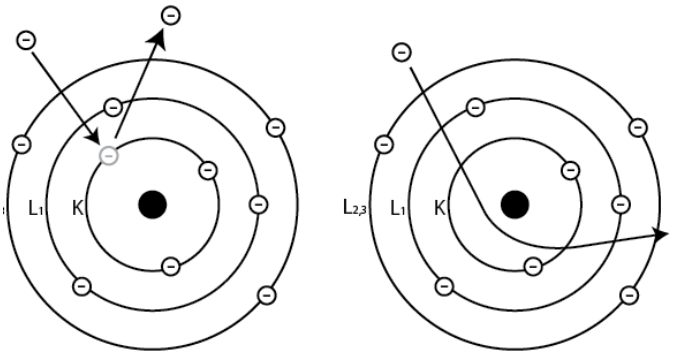

Figure 25: Electron scattering diagram

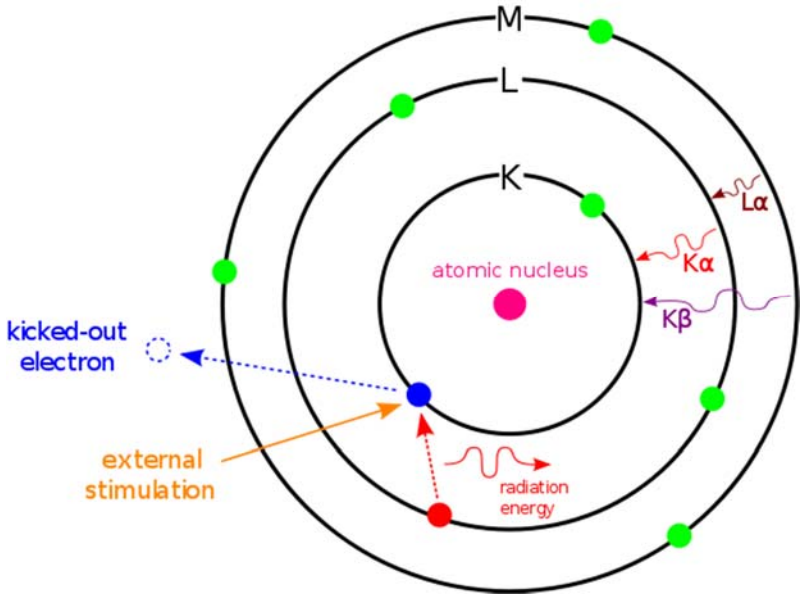

Figure 26: EDX/WDX Characteristic X-ray Generation Diagram

macro scale is the electrons collision with the atom, not the components within the atom. Secondary electrons have only about 3-5eV after their encounter, whereas the backscattered electrons have 60-80% of their incident eV.

For the case of EDX, the electron will collide with an electron within a sample atom and cause a reconfiguration of electrons within the atom to different shells. During the change between shells, x-rays are released to balance the electrons energy of orbital angular momentum with the allowed energy levels within the atom. These characteristic x-rays are detected and analyzed for their relevant information.

Secondary and backscattered electrons are collected by separate detectors. The secondary detector provides a positive charge that attracts the low eV secondary electrons, measuring the intensity and recording it for the location plotted by the system. The results are then re-plotted to an image on a screen, at the same relative coordinates at a viewable size relative to the operator. Backscattered electrons are collected by a detector located very near the source electron beam and is configured to catch only those electrons who eV matches that of an electron that has interacted with the make-up of the atoms in the material. The two configurations can be set to catch electrons are 1. TOPO where the detector selectively collects those that rebound from collisions at the surface to create an image. These images give detailed images of what the surface topography looks like at high orders of magnification. 2. COMPO where the detector selectively collects electrons that have interacted with the atoms internal structure providing details of which areas of the surface contain atoms of heavier or lighter mass based on the electron clouds of the constituents.

The EBSD is a separate detector that has a phosphor screen that the electrons collide against. The sample is set at an angle corresponding to the electron source beamline and the

detector. The ideal angle for the Hitachi High-Tech Science Systems S-3000N Scanning Electron Microscope 50E-5127 with the ThermoScientific EBSD detector is 70º.

The electrons from the source will interact with the surface atoms and rebound at angles based on the surface microstructure. It is therefore prudent to take extra care with surface preparation. Mechanical polishing and lapping will create surface stress in the direction for which material is removed. As a last step in the polishing process, it is necessary to relieve this stress. For our experiment, the samples were subjected to electropolishing. In the electropolishing process, the sample is positioned so that a material selective mild acid is in contact with the surface to be polished. Depending on the material being polished, a potential is applied across the surface so that the acid will selectively attack atoms with high surface energy. These will be the atoms at what would be considered "high peaks" on the surface. This process of removing the "high peaks" in a repetitive manner smooths the surface. In our case where you have mechanical stress induced at the surface, the atoms bound by this stress energy will be one of the preferential atoms that the acid attacks relieving surface stress.

Having removed surface distortions, the electrons in the EBSD configuration interact with the atoms at the surface and their diffracted angles change according to the relative positioning in the material. This produces what are known as Kukuchi lines on the phosphorous detector that the camera images. Kukuchi lines are formed as a result of the structure within the crystal. Clear pathways at specific angles that allow more electrons to diffract and intensify the image at that location. Therefore, the Kukuchi lines can be deciphered into orientation space to determine what the structure is like at a specific point based on the lines and their angles. Stereographic projection is a method of mapping orientation space that was developed to aid in the interpretation of Kukuchi lines. Combined with the scanning principle of the electron

microscope, one can obtain a map of the surface crystal orientation for every x/y coordinate of the samples surface. This data is interpreted into Euler angles, which are the angles from the three axis in the spherical coordinate system.

2.2.4 FE-SEM interface cross section

The Field Emission – Scanning Electron Microscope (FE-SEM) uses an electron source that differs from the mainstream SEM. Typical SEM's use a thermionic filament that is elevated to a high temperature to give electrons the ability to overcome the work function of the material. Field emission sources are configured in a way that a very high potential can be applied to pull the electrons out of the filament. The result is a much higher intensity electron beam with a lower energy spread (0.3-0.5eV) [24]. With higher intensity, energy dispersive spectroscopy (EDS) can provide much more accurate results.

Chapter 3

Results

3.1 Microstructure analysis results

3.1.1 Optical micrography analysis

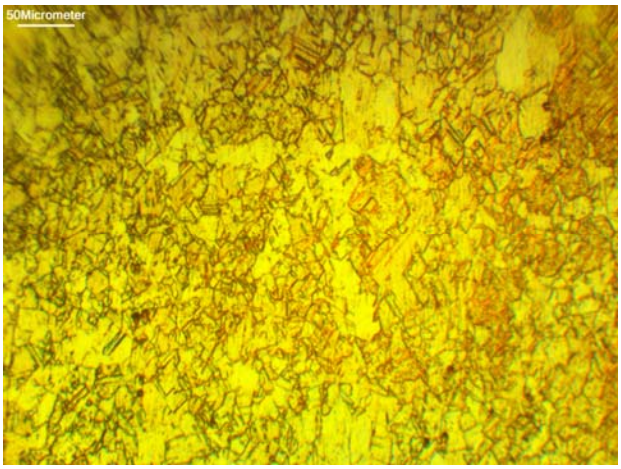

Figure 27: Ferric Chloride etched half hard sample

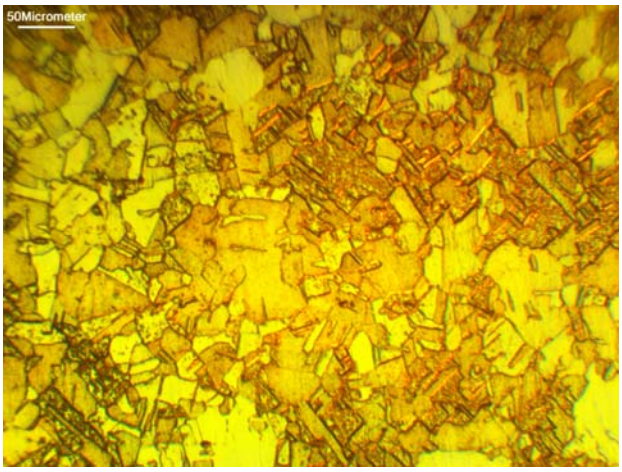

Figure 28: Ferric Chloride etched annealed sample.

Figures 27 and 28 are digital photographs taken of the surface (top down view, normal to what will be the interface of the Al and Cu) of the as received half-hard copper and the same material after annealing at 400°C. The images were taken at 20X magnification. The images were taken prior to Al sputter coating. Each sample was mechanically polished and lapped for smoothness, then exposed to a ferric chloride solution to etch away material at the grain boundaries to provide optical evidence of grain boundaries. Figure 27 shows significantly smaller grains, consistent with a work hardened sample; parallel grain boundary lines indicate the presence of annealing twins consistent with an annealed or hot rolled material. Figure 28 shows larger grain size and annealing twins.

3.1.2 SEM-EBSD results

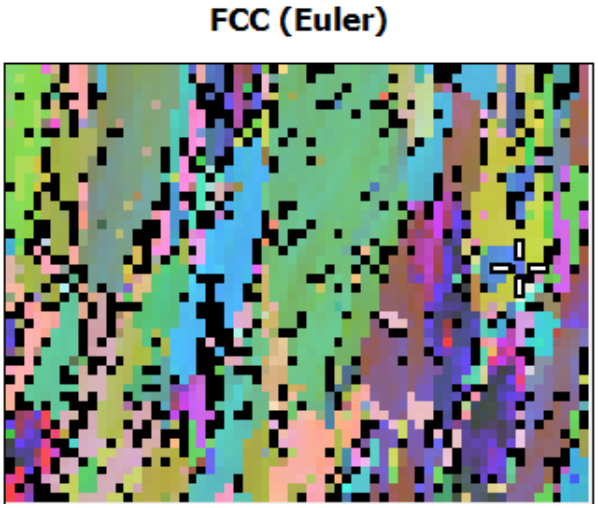

Figure 29: SEM-EBSD Grain mapping Half-Hard Sample

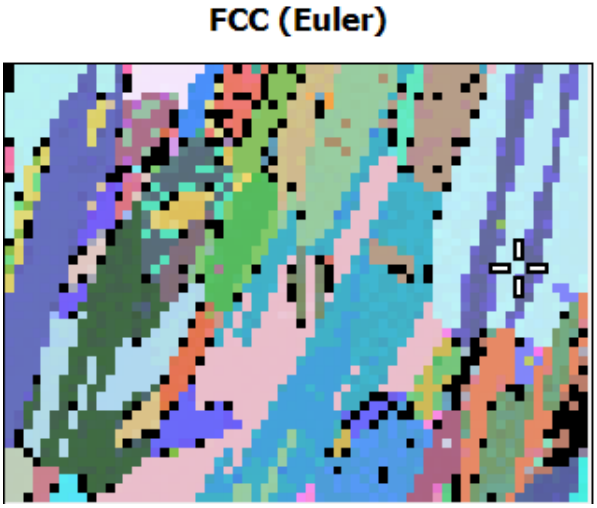

Figure 30: SEM-EBSD grain mapping annealed sample

Figures 29 and 30 are images of the surface (top down view, normal to Cu-Al interface) of the as received half-hard copper and the same material after annealing at 400°C. The magnification is 900X. The images were taken prior to Al sputter coating. In these FCC (Euler) images, the analysis software deciphers the Kukuchi lines created observed by the detector to determine what the crystal orientation is at the surface for each individual pixel shown. Each color represents a specific FCC orientation. A black pixel represents a location that the structure was indeterminate with respect to an FCC orientation. The asymmetric lengthening of the grains indicates the rolling direction of deformation during the hot rolled process. As with the optical micrography, it can be seen that the grains in the pre-annealed sample are larger than the as received sample. Fewer indeterminate pixels in the pre annealed sample indicates that recrystallization / grain growth has begun to assimilate disorder present in the grain boundaries, creating order and reducing structural indeterminacy.

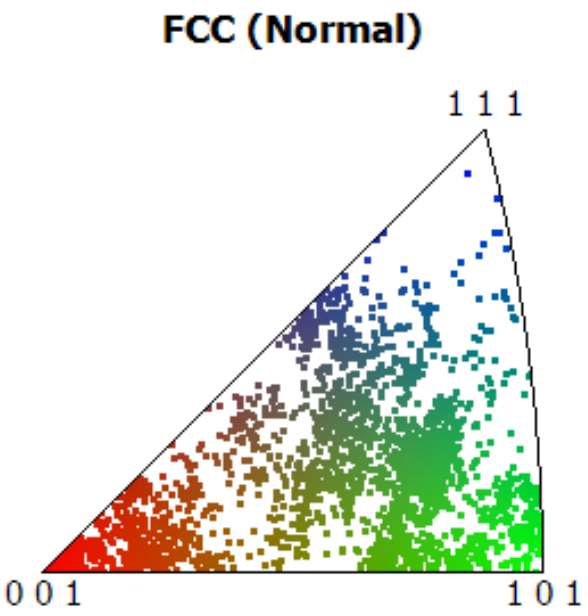

Figure 31: SEM-EBSD Euler Angle map Half-Hard Sample

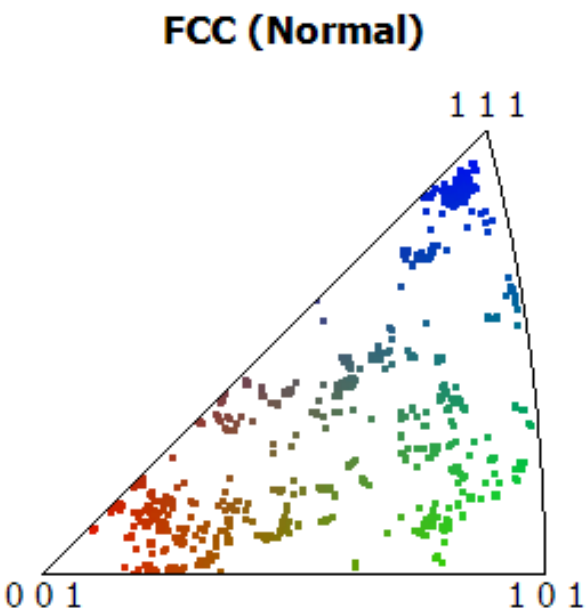

Figure 32: SEM-EBSD Euler Angle map annealed sample

Figures 31 and 32 show the EBSD data in stereographic projection looking down the axis of normal to what will be normal to the interface between the Cu and Al. This is the same data from figure 29 and 30 presented in an alternate fashion. Each dot represents a crystal orientation detected. The half-hard sample shows many more grains, one dot equals one grain detected; the pre annealed sample shows fewer. The half hard sample shows many crystal orientations in the (001) general direction and few in the (111) direction. This is consistent with an FCC roll deformed sample where the slide plane with lowest deformation energy turns inward to facilitate easier deformation. FCC (111) slide plane has the least energy so as these planes turn inward, the count decreases and (001) increases as the edges of the crystals become oriented to normal. The pre annealed sample shows that these (001) planes have relaxed, and crystals with the (111) orientation grow.

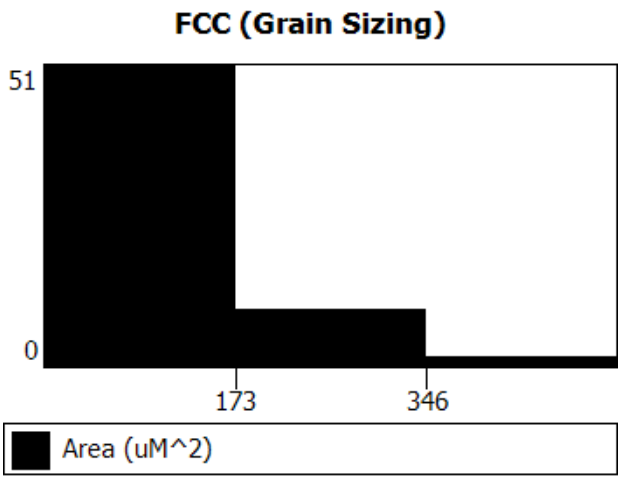

Figure 33: SEM-EBSD Half-Hard Sample

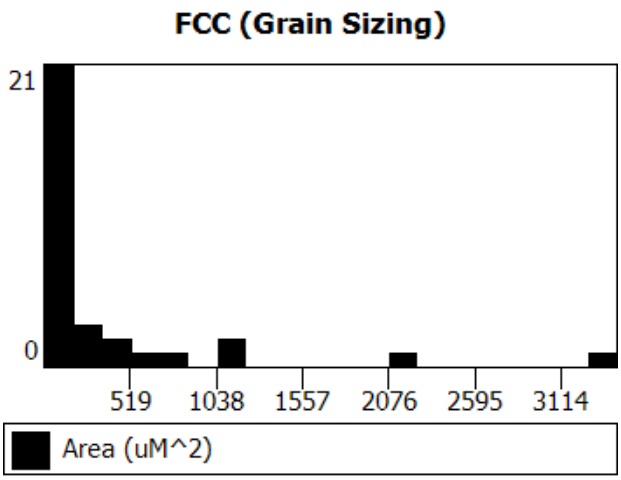

Figure 34: SEM-EBSD annealed sample

Figures 33 and 34 show the EBSD data as a numerical count of surface area grain size. The lower axis differentiates each grain by its approximate surface area normal to what will be the Cu – Al interface. This is the same data from figures 29 and 30. The Y axis of the graph shows the number of counts of a grain with surface area size represented along the X axis of the graph. It can be seen that the half hard sample has more grains of a smaller size and the pre annealed sample has fewer grains with larger size.

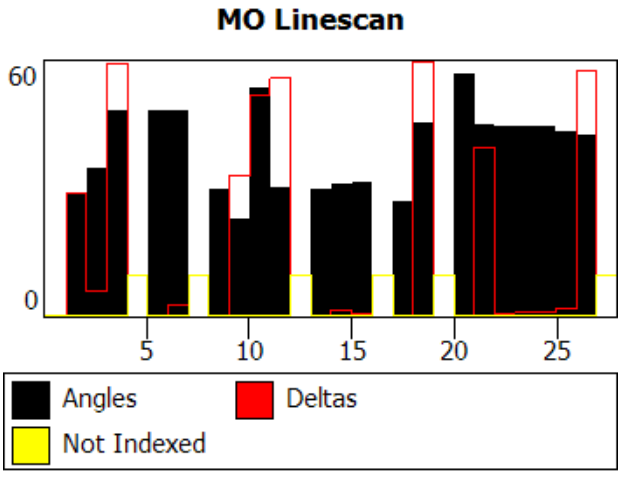

Figure 35: SEM-EBSD Half-Hard sample

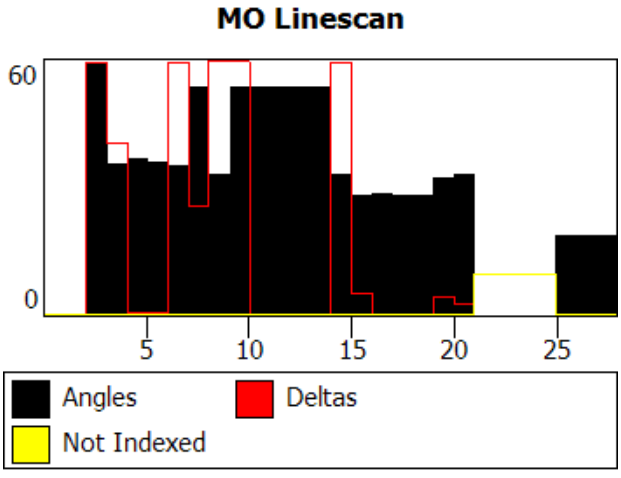

Figure 36: SEM-EBSD Annealed Sample

Figures 35 and 36 show the EBSD data from figures 29 and 30 highlighting the misorientation between grains. The software draws a straight line and tabulates the euler angle change in crystal orientation along that line. When it encounters a change in crystal direction, it calculates the change in angle from the last grain to the new grain and from the new grain to the first grain. The Y axis is the number of counts for each difference. In units of degrees, the black lines indicate the misorientation between the crystal at the beginning of the line compared to the current position and the red line indicates the difference in angle between the previous position on the line and the current position. The yellow line indicates the count of misorientations not indexed. A non-zero count on the yellow line, showing greater than 10 counts, indicates that there was no indexing at this angle. This information is consistent with a FCC metal with higher stacking fault energy that has been hot rolled. In hot rolling, crystals annihilate as unstressed crystals form. Angles between crystals will be lower in a hot-rolled sample than they will be in a cold rolled sample[13].

Much of the EBSD data is redundant, but it is necessary to have a complete understanding of the interface before sputtering as the opportunity to analyses after the fact becomes problematic.

3.1.3 Microhardness test results

Figure 37: Microhardness test Half-Hard Sample

Figure 38: Microhardness Test annealed Sample

The microhardness test is a less important measurement of the interface of the samples but verifies that the amount of microstructure in the sample beyond the surface has been reduced. The Vickar's hardness indicated shows that the annealed sample has half the hardness of the work hardened sample.

3.2 Interface reaction results

3.2.1 SEM cross section profile

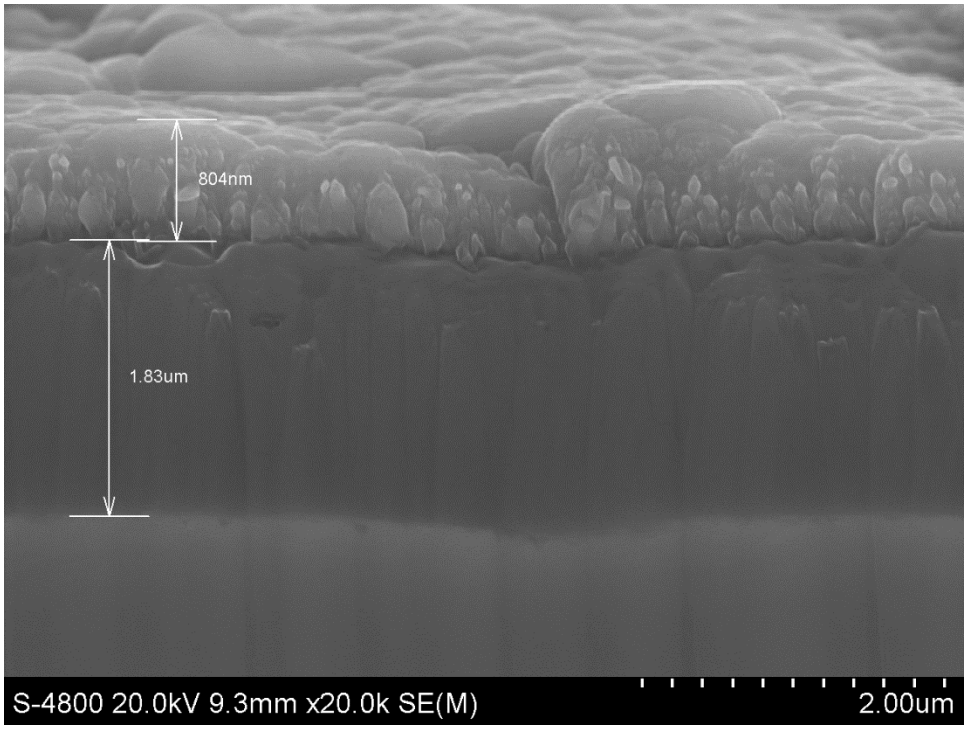

Figure 39: FE-SEM Pre Aged Al-Cu Cross section Interface after ion milling

In figure 39, the image is of the cross section view of the Cu – Al interface, with the Cu on the bottom, the darker area in the middle being the Al and the surface oxide. The sample is the pre annealed sample, meaning that the Cu was annealed before the Al sputter coat was applied to the mechanically smooth interface. This image was taken to verify the depth of the sputtered Al and to inspect the interface for pre aging conditions. At the time this image was taken, the sample had rested for approximately two months allowing the formation of Al_2O_3 on the surface. Ion milling of the cross section was performed right before the image was taken. This method of exposing the cross section insured that additional external stress wouldn't introduce additional defects to the interface.

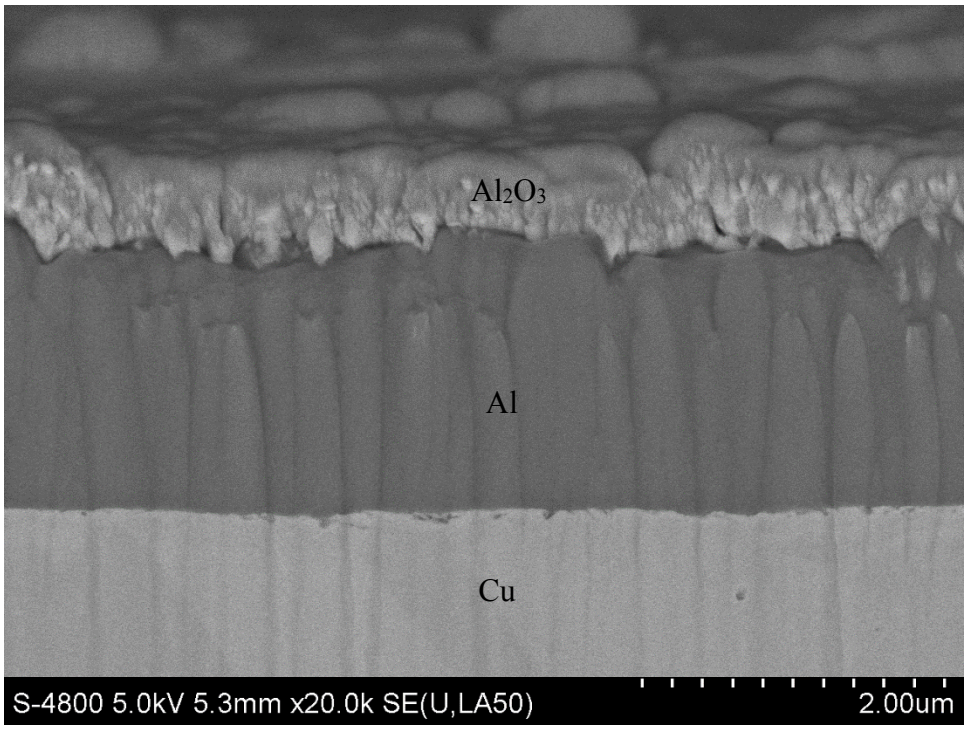

Figure 40: FE-SEM Pre Aged Al-Cu Compositional map after ion milling

Figure 40 is a supplemental image of the pre aged Cu – Al interface with the addition of back scattered electron (BE) composition added in (LA50). The Cu appears bright due to an increased density over that of Al to reflect secondary electrons (SE), and the BE contribute to the brightness because Cu is the heaviest element present. The Al is less dense and a lighter element, so both SE and BE will be darker due to fewer electrons collected. The top layer is Alumina (Al_2O_3) which acts as an insulator. In the conductors, the extra electrons are drained away to the ground, but the insulator builds up a charge due to not being able to drain the elections away. This charge will slowly dissipate electrons at all surfaces in a manner that is collected by the SE detector. Therefore the area will appear brighter due to the volume of electrons not conducted to the ground but collected by the SE detector.

The interface between the Cu and Al appears to have voids, but they do not appear to be a part of the interface itself, merely in the proximity to the interface.

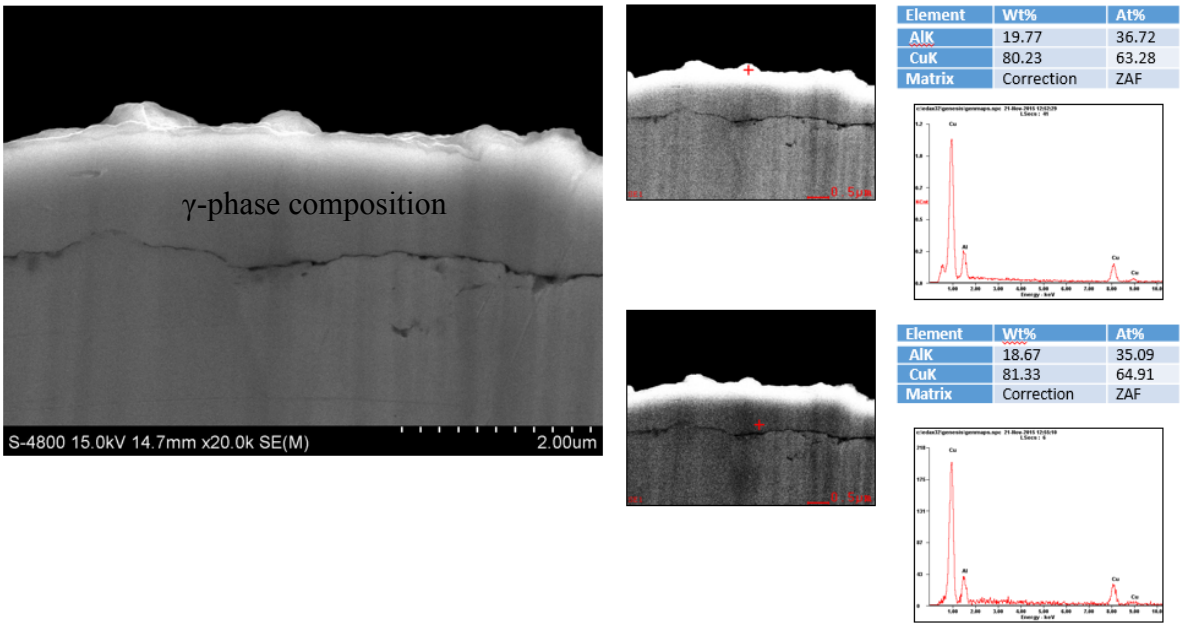

Figure 41: FE-SEM γ-phase region identification by EDS compositional analysis

Figure 41 is a cross section image of the Cu – Al interface after aging at 450°C for 10 hours. The sample was the pre annealed mechanically smooth interface sample. EDS analysis was performed on the area above the boundary feature and below. Figure 41 contains the data for the area above. The smaller subset pictures contain a red cross that represents the target where the composition listed to the right was taken. At the area close to the surface of the sample, the composition shows to be in the range of 61-69 at. % Cu, which is the composition of the γ-phase IMC. The lower set of image and stats was taken near the boundary but still above it. The composition also shows to be appropriate for the γ-phase IMC.

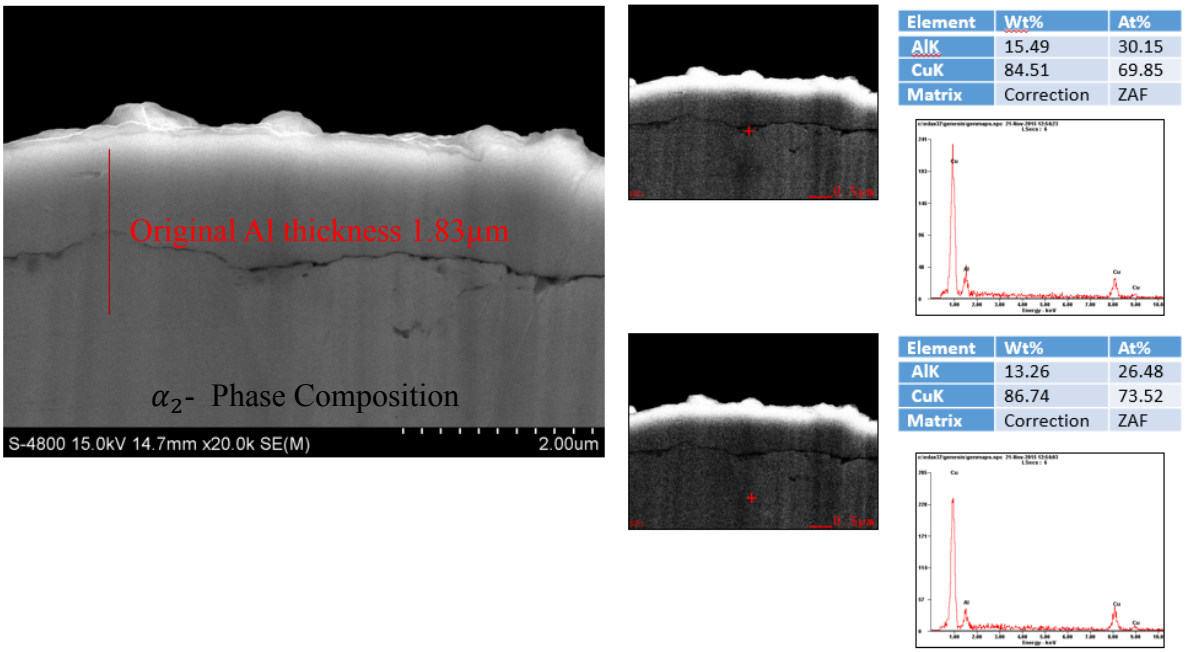

Figure 42: FE-SEM EDS Cu-α_2-phase region identification by EDS compositional analysis

Figure 42 is the second half of data from figure 41, showing the composition just below the boundary and deeper in to the boundary. The compositions show values greater than the 69 at. % Cu, indicating that it is no longer the γ-phase IMC but something different. The magnification and instrument settings have been set the same as the pre aging images in order to do a more accurate comparison of before and after. A red line has been placed on the image showing the original depth of the Al in order to determine whether the boundary is the original Cu – Al interface or an interphase boundary between two phases. The boundary appears to be much more erratic than the interface boundary and is about a third closer to the surface than the original interface. In this image, the voids present appear to be a part of the interface as opposed to just being in the proximity.

3.2.1 XRD results

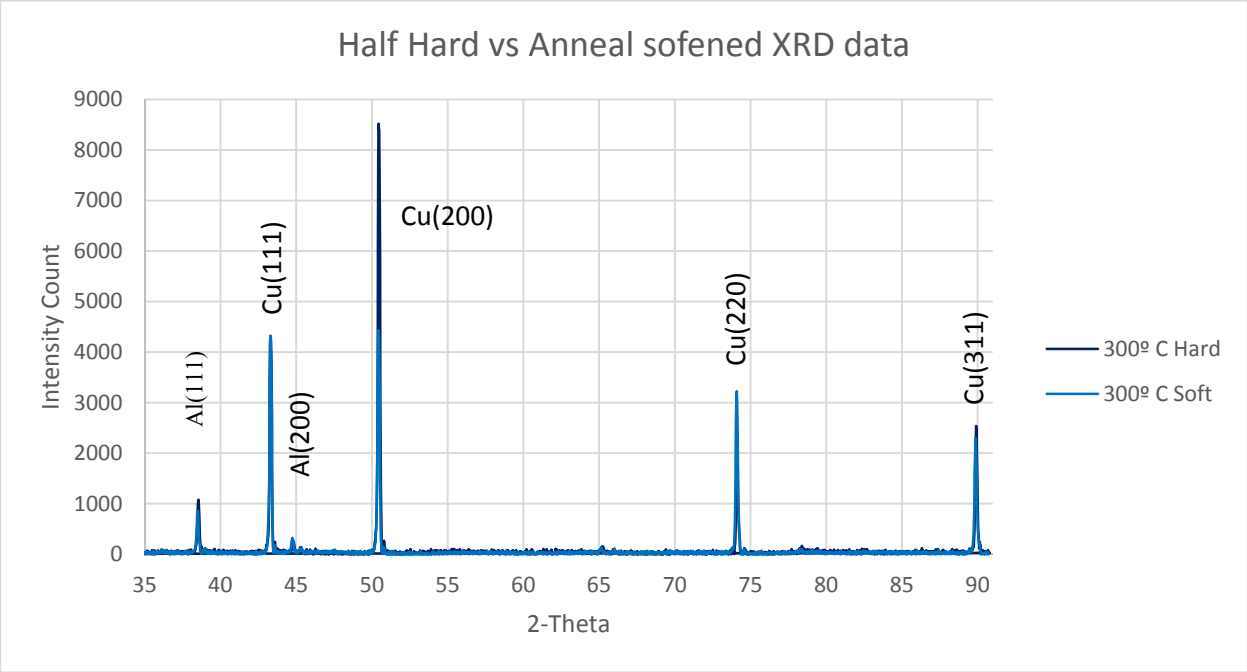

Figure 43: XRD Data, Full range, Half-Hard vs Anneal Soft, aged at 300ºC 10 hours.

Full range scans of 10° 2θ to 120° 2θ were performed and found to contain little more comprehensive data than the shorter 35°-90° 2θ. ICDD data was collected for a wide range of possible structures that could form and a close up range of 42°-45° 2θ was selected as the ideal range for detecting a majority of the possible developing structures. Figure 43 shows what we are calling the 'full range', meaning the larger range that contains the structures we are interested in. Each of the following graphs will show two data sets in a similar color. The lighter color is the pre annealed mechanically smooth sample, abbreviated as soft opposing the 'hard' designation for the mechanically work hardened sample. As colors move from blue to red denotes the temperature increase for comparison in the final graphs. Calculated peaks are identified above or near the specific location. Figure 43 shows proper intensities for Cu and Al with no apparent peaks from any of the other IMCs or oxides.

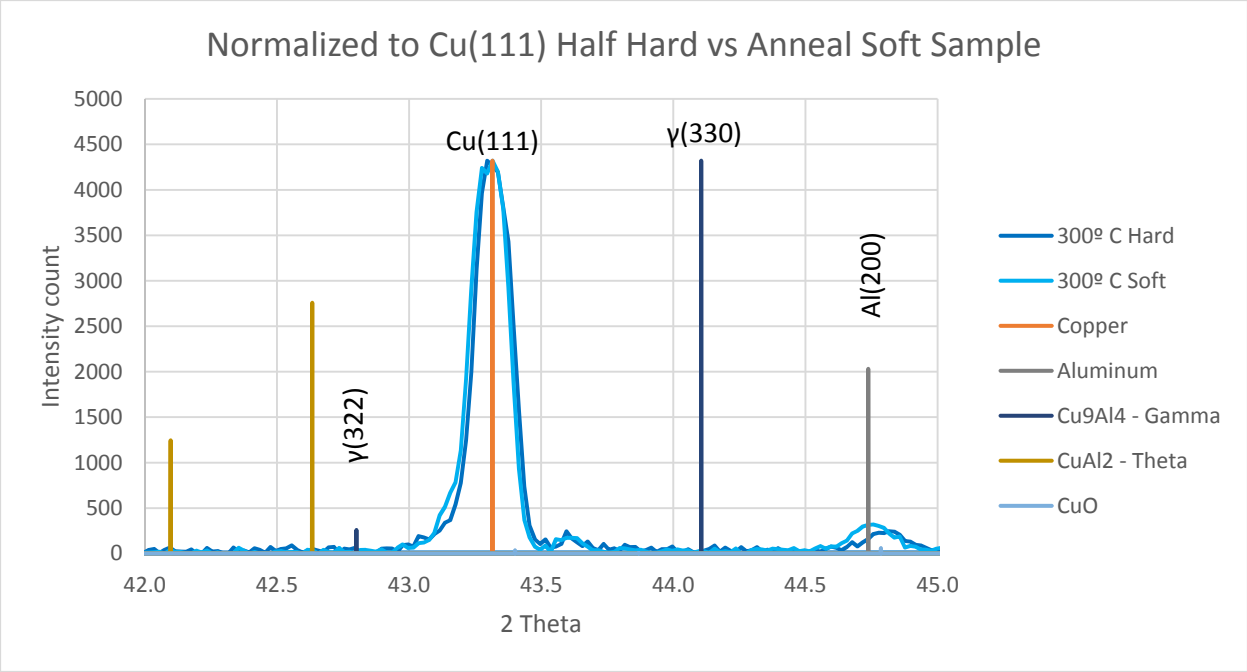

Figure 44: XRD Data, (42°-45°) 2θ range, Half-Hard vs Anneal Soft, aged at 300°C 10 hours

Figure 44 shows the close up range of 42°-45° 2θ with data sets for the low temperature, 300°C aged for 10 hours. Included also are the five possible structures that we might expect to find in our sample that all have signatures that should appear in this range. The first peak we expect to see, based on literature[29], is θ-phase (Theta $CuAl_2$). Consistent through all of the graphs contained herein is normalization to the Cu (111) peak. The small signature to the right of the Cu (111) peak is consistent with what is typically seen when grain twinning is present[15]. The peaks for Al are slightly to the right of where they are calculated and empirically recorded at indicating a small amount of interplanar compression by Bragg's law. There appears to be no signature of formation for either θ-phase or γ-phase.

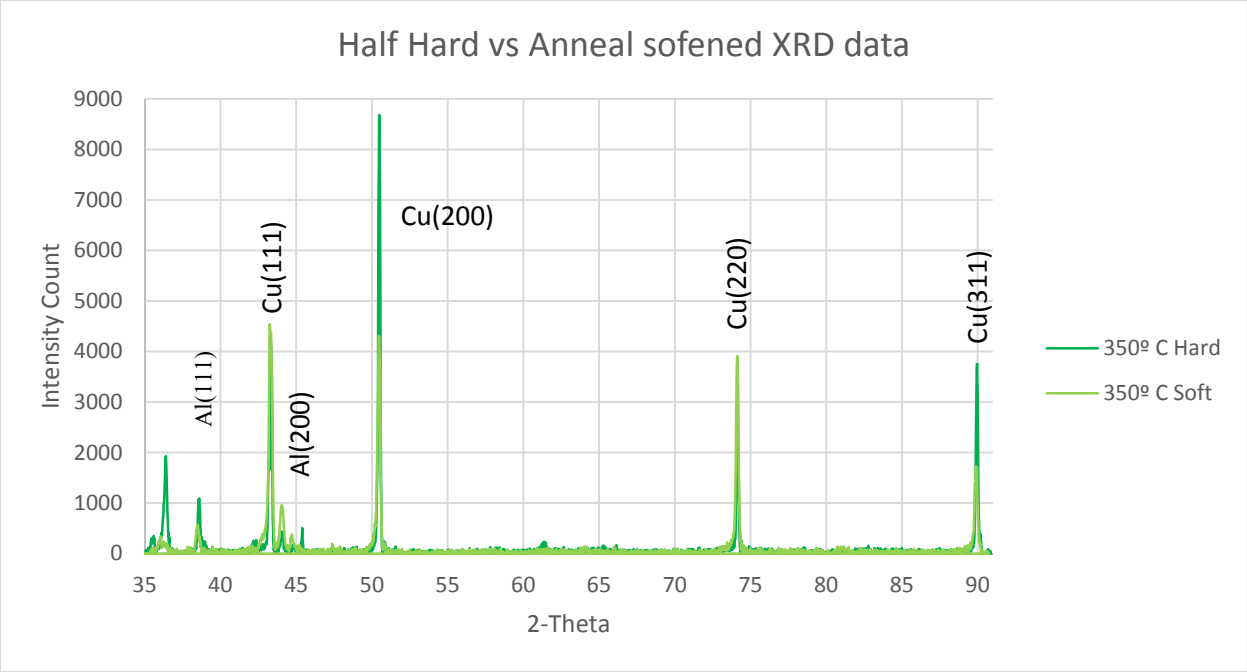

Figure 45: XRD Data, Full range, Half-Hard vs Anneal Soft, aged at 350ºC 10 hours.

Figure 45 compares the half hard and pre annealed (soft) samples aged at 350°C for 10 hours. A signature at 36.3° 2θ on the half hard sample matches with a peak empirically reported in the ICDD for CuO. This particular sample had a portion of the Al thin film broken away exposing the bare Cu surface for a period of time. Therefore, the history of the sample and the peak identified are consistent with the possibility of the formation of Cupric Oxide. A detail that is present in both the 300°C and 350°C sample is that the (200) plane intensity in the hard sample is significantly higher than the counterpart soft sample. This indicates a higher count of planes with that orientation normal to the surface. This is a detail that we observed in the SEM-EBSD analysis. Counter to this, the Cu (111) peak intensity is higher in the soft sample, which also correlates to the SEM-EBSD analysis.

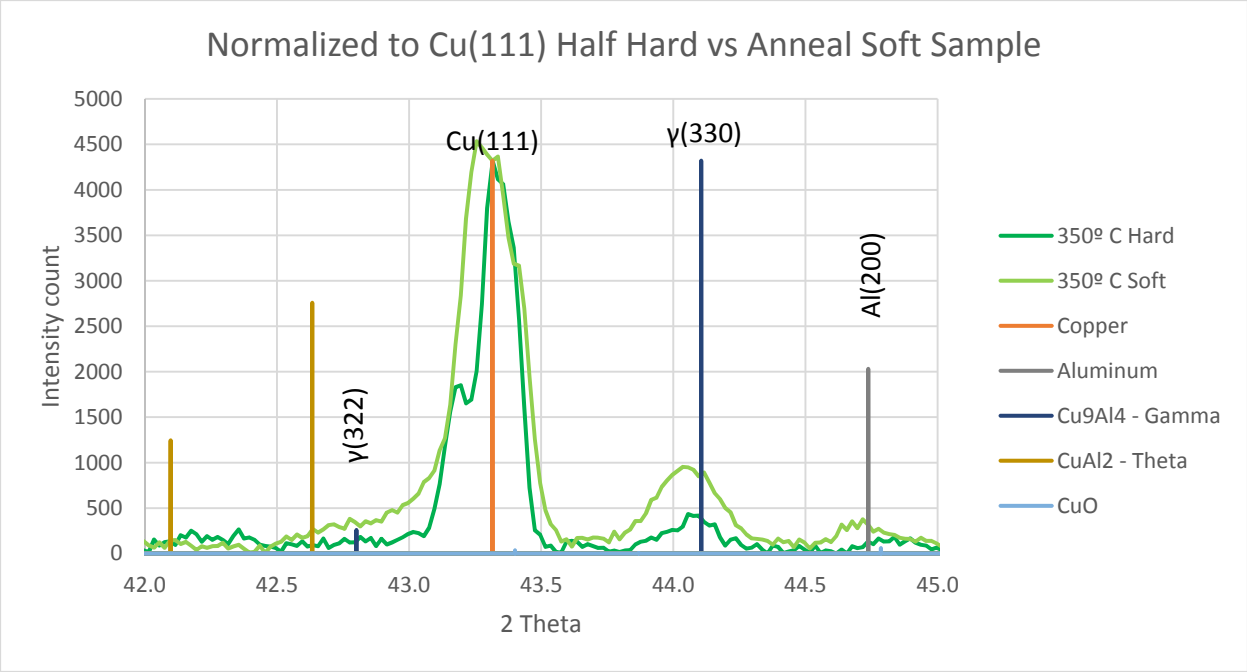

Figure 46: XRD Data, (42°-45°) 2θ range, Half-Hard vs Anneal Soft, aged at 350°C 10 hours.

Figure 46 shows the close up range from 43° to 45° 2θ. Data sets for the half hard sample in the darker green and the pre annealed soft sample in lighter green with the other possible structures that could be present. Beginning at the left is an increase in the background that could indicate a small portion of θ-phase but not enough to be any significant formation. The half hard sample shows a small side peak on the left side that is unique to this sample and not observed in any other sample. Therefore it cannot be concluded what it is the result of. Both of the Cu(111) peaks show broadening, more than the 300°C sample, with slightly more broadening to the left indicating an expansion of some of the planes. The γ-(330) peak is beginning to grow, with more growth in the soft sample than the hard. The Al (200) peak is still present, compressed in the hard sample (peak position right) and normal in the soft sample.

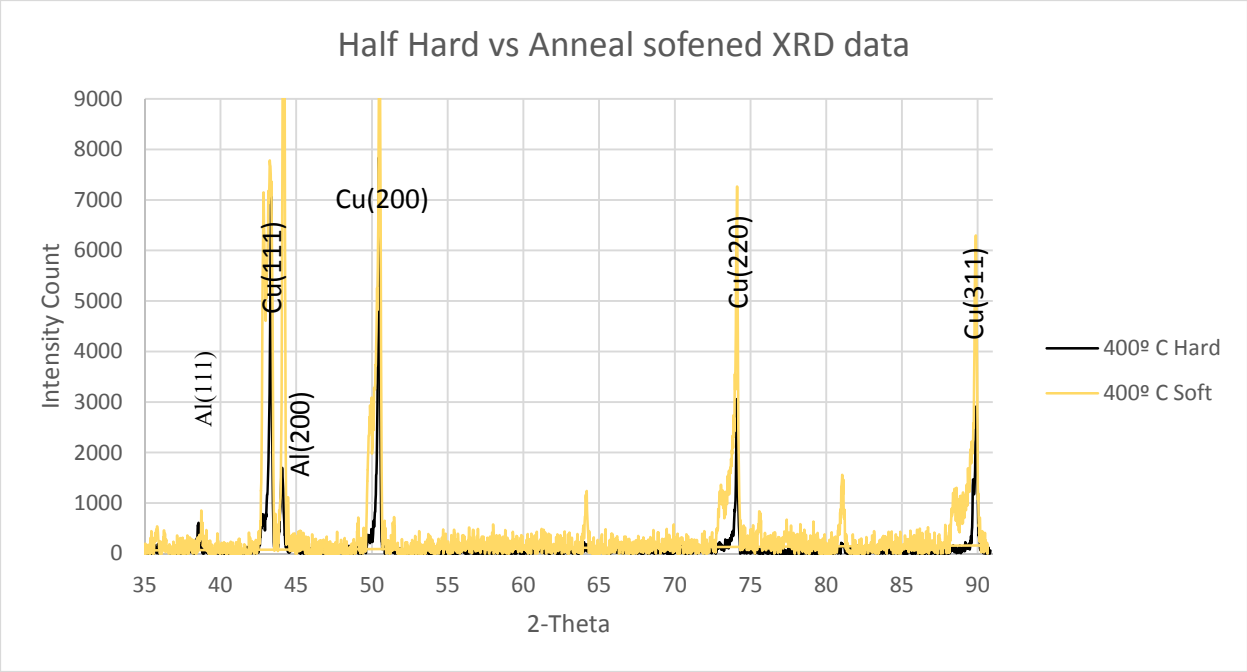

Figure 47: XRD Data, Full range, Half-Hard vs Anneal Soft, aged at 400ºC 10 hours.

Figure 47 shows the full range scan for the samples aged at 400°C. As the data sets move towards the hotter temperatures, yellow range colors were used for this step, but in order to more clearly show the contrast between the hard and soft, the half hard color has been changed from gold to black for this graph. It is in this graph that we first begin to see the side peak growth on all of the Cu peaks. It is also observed that this side peak and left side Cu peak expansion is much more pronounced in the soft sample than in the half hard sample. New peaks at 64° and 81° 2θ are consistent with empirical data from the ICDD for γ-phase. Now that three peaks for γ-phase have been identified, it can be more easily concluded that the phase growing is the γ-phase. Al structure still seems to be present by the peaks at Al (111) and Al (200). γ-phase and CuO have peaks very close together at 35.89° and 36.3° 2θ. This is too close together to definitively distinguish but based on the sample surface and the presence of other γ-phase peaks, it is more likely to be γ-phase.

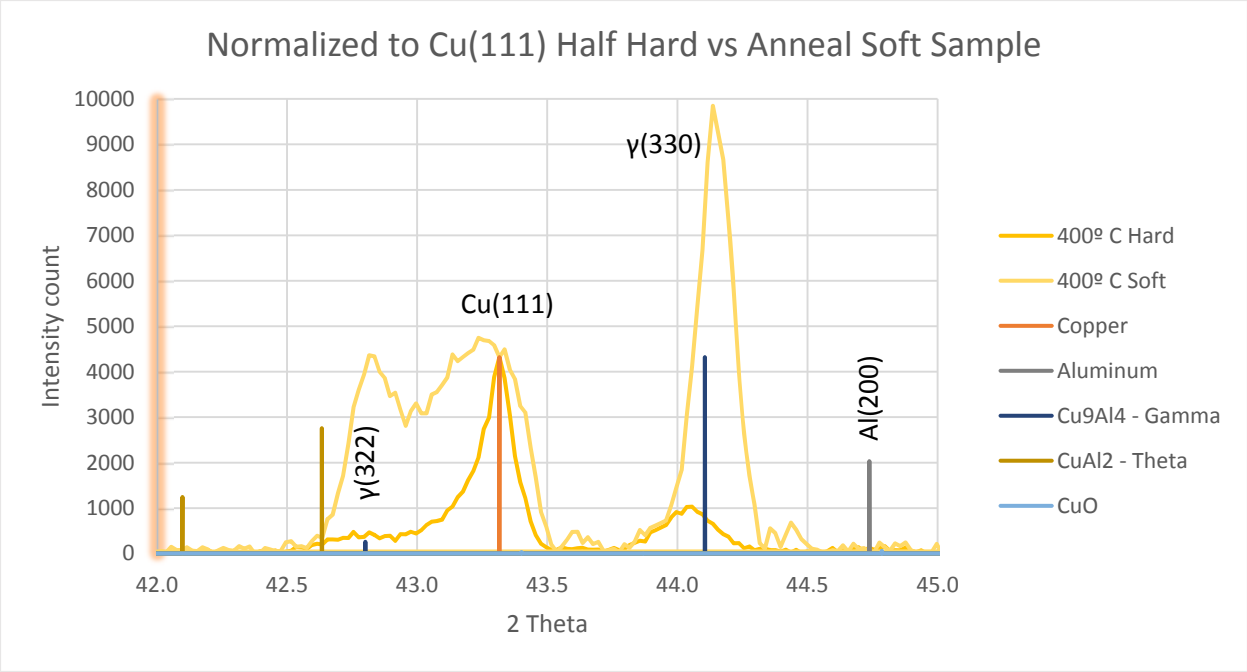

Figure 48: XRD Data, (42°-45°) 2θ range, Half-Hard vs Anneal Soft, aged at 400°C 10 hours.

Figure 48 shows the close up range of 42º-45º 2θ for the samples aged at 400ºC for 10 hours. A reddish highlight has been applied to the left axis to indicate that the scale has changed from the previous graphs to accommodate the γ (330) peak that grew significantly in this test. From left to right, there does not seem to be any growth of the θ-phase as expected. There is a peak over what would be the γ (322) but this peak resembles peaks growing to the left of all of the Cu peaks in position and ratio too much and is growing at a different rate than the other γ-phase peaks. Therefore it is concluded that it is most likely not γ (322). The Cu (111) soft peak has a large amount of asymmetric peak expansion to the left indicating interplanar expansion on a gradient. The γ (330) peak has grown significantly in the soft sample and has become compressed by its right peak position. The hard sample has grown some. The Al (111) peak is virtually gone indicating very little pure Al left on the surface.

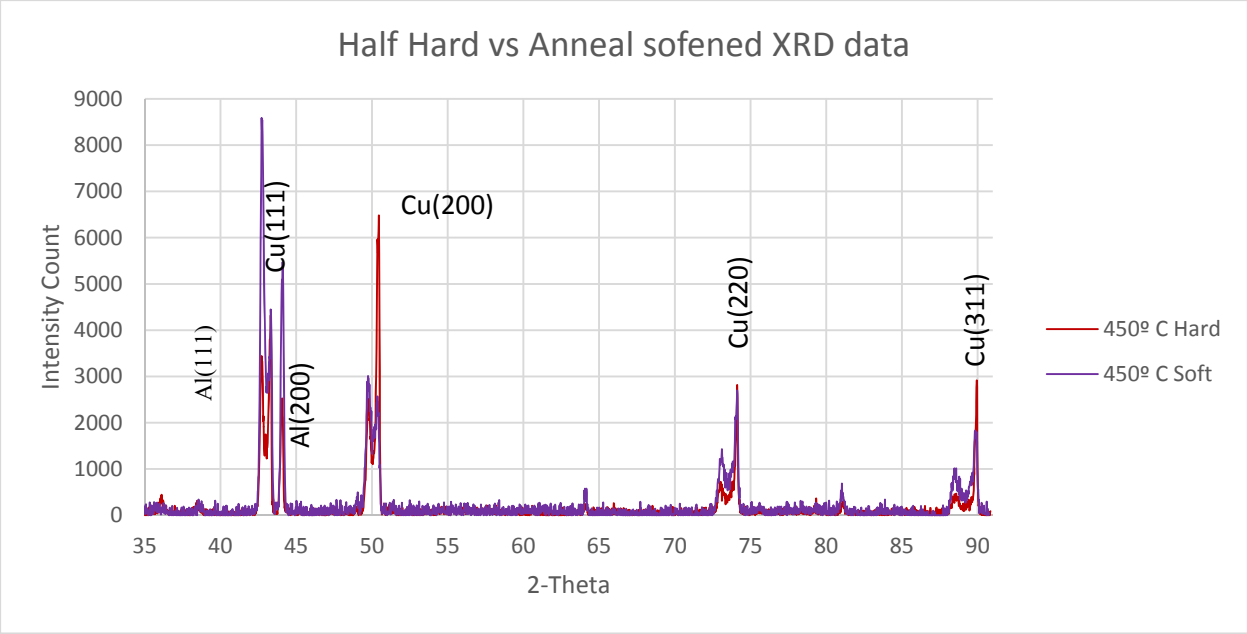

Figure 49: XRD Data, Full range, Half-Hard vs Anneal Soft, aged at 450ºC 10 hours.

Figure 49 shows the full range scan of the hard and soft samples aged at 450°C for 10 hours. In order to better show the contrast of the two samples data, the normally softer color of the soft sample has been changed to purple for this graph. At 450°C, we see even more growth of the Cu side peaks and we also see the formation of the side peaks in the half hard sample as well. We see more growth of γ-phase in the soft sample than we do in the half hard sample due to the peak intensities. There appears to be little if any Al structure left by the peaks at Al (111) and Al (200).

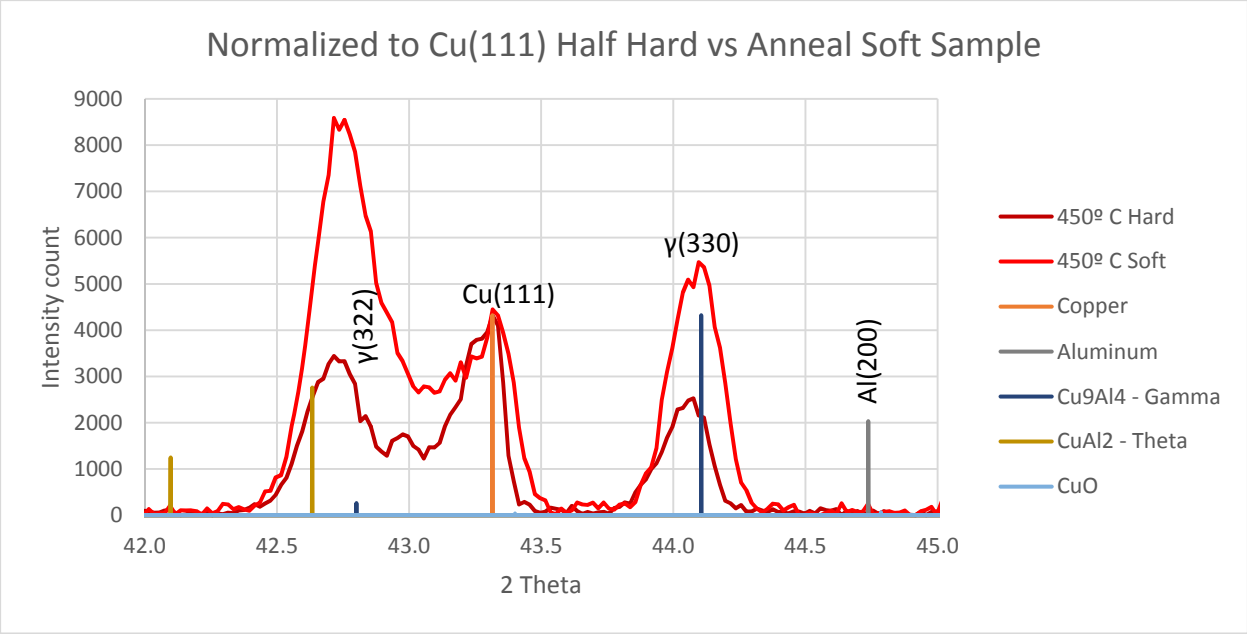

Figure 50: XRD Data, (42º-45º) 2θ range, Half-Hard vs Anneal Soft, aged at 450ºC 10 hours.

Figure 50 shows the close up, 42º-45º 2θ view, of the hard and soft samples aged at 450ºC for 10 hours. From left to right, we still see no development of the θ-phase structure. It can be more clearly seen that the peaks at ~42.75° 2θ are not θ-phase or γ-phase. Broadening of the Cu (111) half hard side peak seems to be symmetric whereas the soft sample right side broadening is convoluted with the left broadening of the Cu (111) peak. The γ (330) soft peak has dropped significantly and its position is more centered if not a bit expanded to the left. The half hard γ (330) peak is moderate in size, comparable to the growth rate of the 400°C sample. No Al structure appears to remain by the peak intensity of the Al (200) signal.

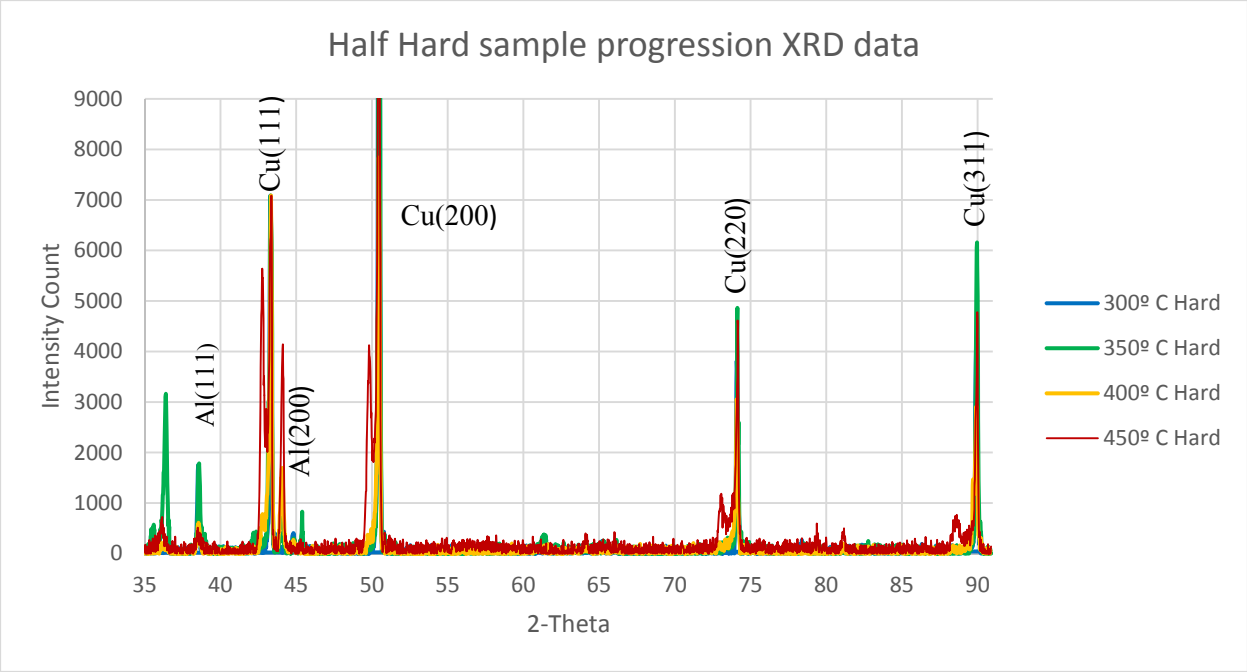

Figure 51: XRD data, Half Hard samples, Full Range Scan, temperature progression.

Figure 51 puts together all of the half hard samples at the various temperatures for comparison. The first observation at the left is the cupric oxide peak at 36° 2θ in green on the 350°C sample as discussed above. The Al peaks are present at the lower temperatures and gone at the higher temperatures. The left shoulder expansion of all four Cu peaks and eventual appearance of the Cu left side peak is consistent and proportional. It would appear that once the temperature exceeded the 400°C temperature that the soft sample had the Cu pre annealed before aging at, the Cu side peaks accelerate in growth.

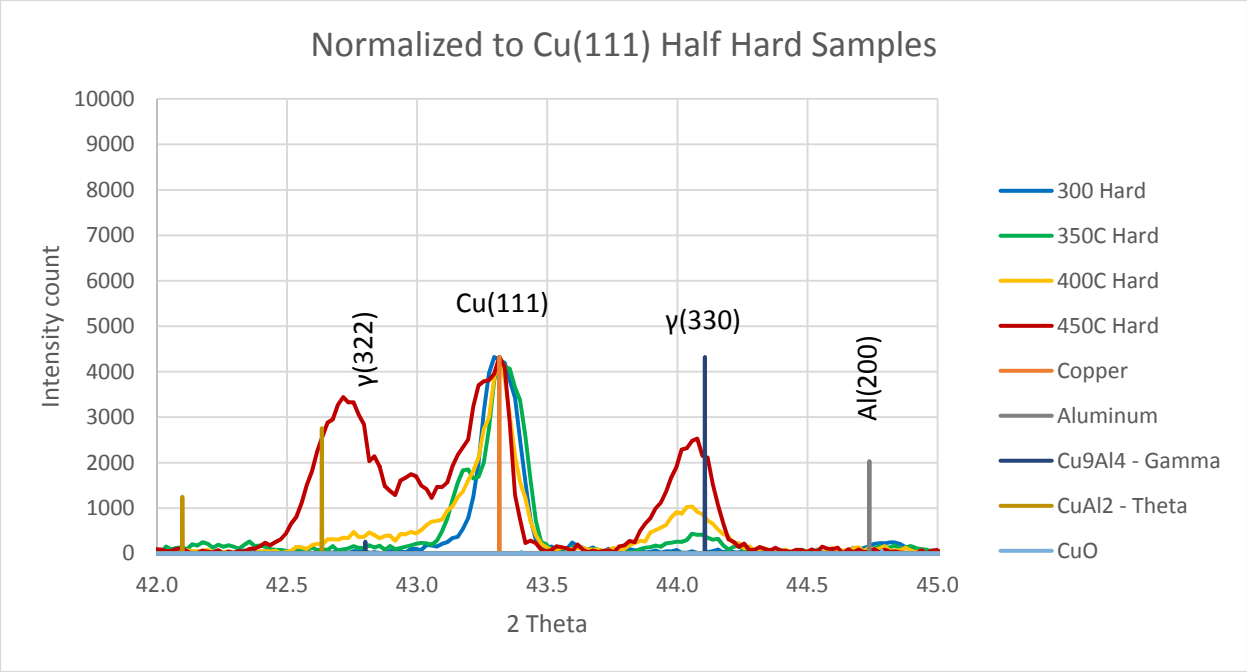

Figure 52: XRD data, Half Hard samples, (42°-45°) 2θ range, temperature progression.

Figure 52 is a comprehensive close up, 42°-45° 2θ range, of all of the hard samples. This graph shows the clear progressive growth of the γ (330) peak. The diminish of the Al (200) peak and the asymmetric left side expansion of the Cu (111) peak with the development of the left side peak. The position of the Al (200) peak shows that it remains slightly compressed throughout all of the tests. The γ (330) peak shows by its position that it is under slight tensile stress throughout all the tests. Finally, the Cu (111) side peak shows a significant acceleration in growth beyond the 400°C temperature.

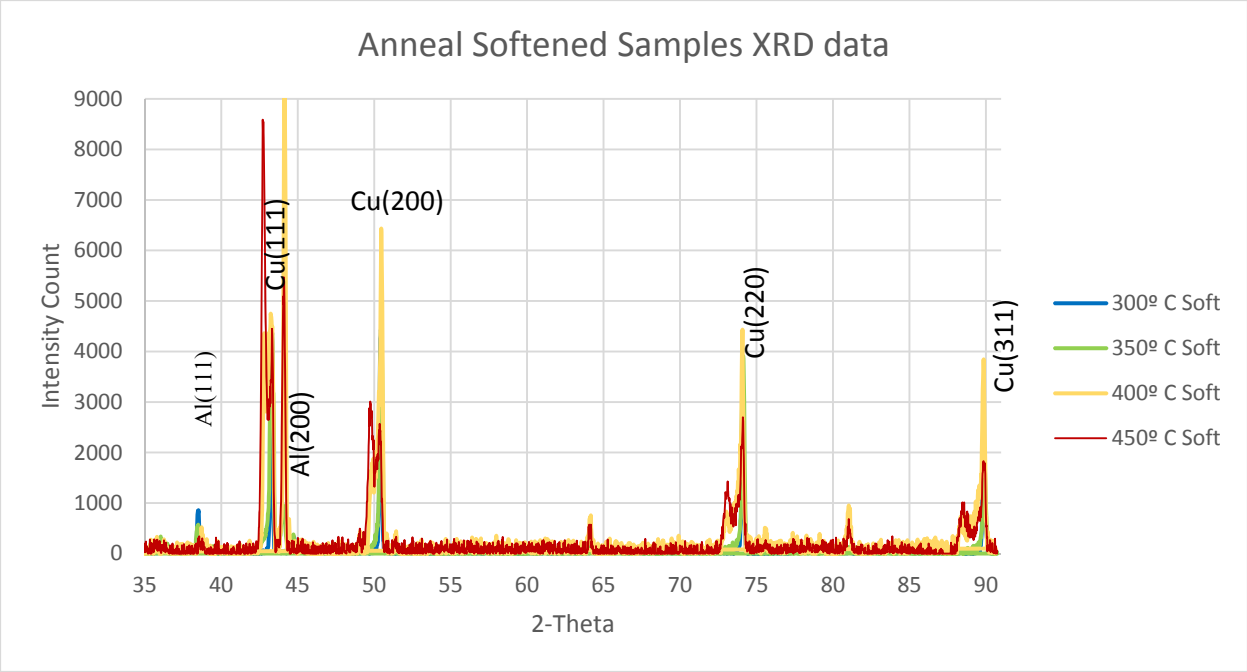

Figure 53: XRD data, Anneal Softened samples, Full Range Scan, temperature progression.

Figure 53 shows the full range scan of all of the soft samples compared against each other to highlight the growth of γ-phase and the asymmetric expansion of the left side of the Cu peaks with the development of the Cu left side peak. Progression is very consistent and logical for all signatures. There appears to be nothing inhibiting the process by the smooth development of each feature that has already been described in previous graphs.

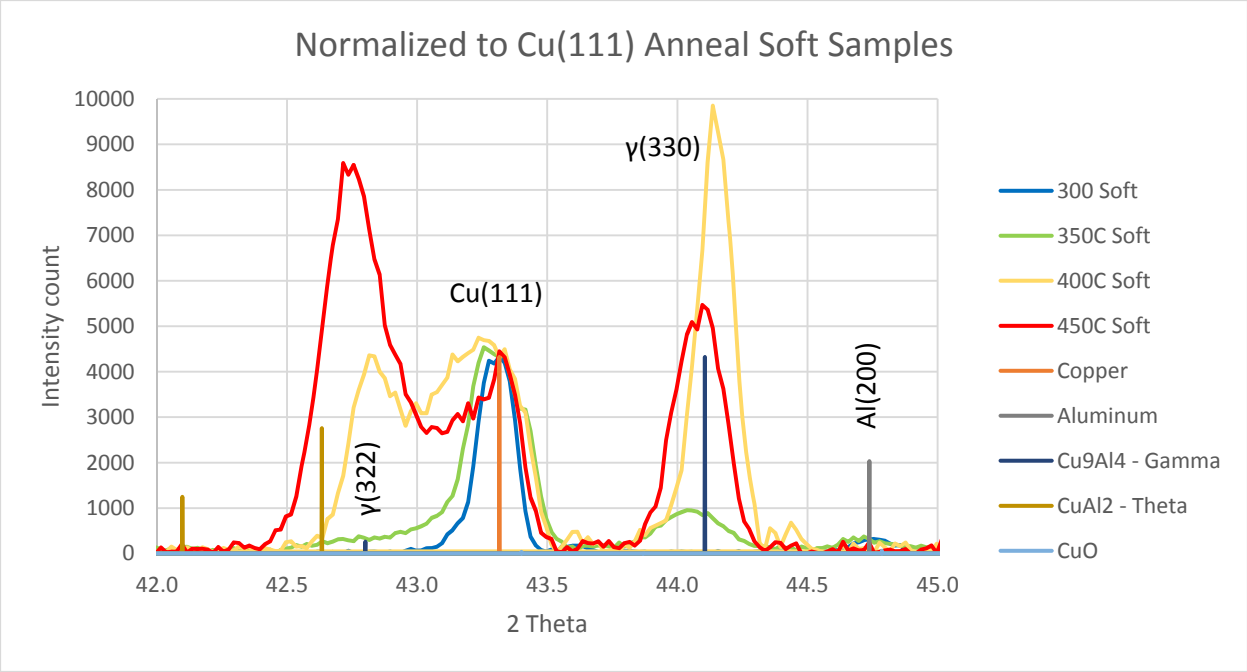

Figure 54: XRD data, Anneal Softened samples, (42°-45°) 2θ range, temperature progression.

Figure 54 shows the close up, 42°-45° 2θ range, of all the pre annealed soft samples. The progressive growth of γ (330) appears to be exponential until the Al supply is exhausted and then the development of the Cu (111) side peak appears to consume some of the γ-phase. The peak position of γ (330) begins somewhat expanded at 350°C and becomes compressed when it goes through its rapid growth at 400°C. It appears that once its growth is reversed, the stress is relieved and it settles in the empirically recorded position. By its peak position, the left side peak appears at 400°C somewhat compressed, if you take its average position throughout the data sets. At 450°C the position seems to be more normal to the average.

Chapter 4

Discussion

4.1 Optical Micrography

For full evaluation of the final experiment, it was necessary to have a thorough understanding of the surface microstructure that would impact the interface dynamics after sputtering. Optical micrography allowed us to correlate data obtained by SEM-EBSD for logical accuracy. The results of the optical micrograph microstructure analysis showed the presence of annealing twins in the as received material. In the second sample, after annealing, the optical micrographs showed a distinct growth in the grain sizes, with continued crystal twinning. This difference confirms that the density of grain boundaries at the interface had been reduced. This opportunity for pipeline diffusion via grain boundaries and dislocations will be reduced in the annealed sample.

4.2 Discussion: SEM – EBSD microstructure analysis of un-sputtered Cu

The SEM-EBSD FCC Euler grain mapping of the as received material shows elongation in the crystals, consistent with a roll deformed material. The annealed sample still indicates the presence of the preferred rolling texture, but shows fewer unreadable locations. The as received sample shows a larger number of black spots that indicate an area where the Euler angle could not be determined. This is not unusual at grain boundaries where the structure is indeterminate. The annealed sample shows fewer because recrystallized grains were in the process of growing into neighboring grains. This process first assimilates the atoms at grain boundaries, closing gaps and reducing the amount of indeterminate structure.

The Euler map of the as received sample shows a greater number of registries consistent with a greater number of grains in an area the same size. There are a greater number of registries

around the {001} orientation and fewer with the {111} orientation. This is consistent with a rolled FCC material. During the rolling process, the lowest energy glide planes are pushed into an orientation to ease the flow stress of deformation. In an FCC material, the {111} glide plane is the lowest energy. As a result of rolling the, {001} edges of the unit cell will tend to orient toward the surface, and the cross cube {111} planes orient more perpendicular to the surface. The annealed sample shows fewer registries consistent with a larger number of grains. As stress was relieved in the annealing process, and nucleated stress free grains grew in unrestricted directions, more grains with the {111} plane appeared oriented to the surface, and the number of planes with the {001} orientation was reduced.

The grain sizing report is consistent with the micrography showing fewer larger grains after annealing. The misorientation line scan is consistent in that it shows a movement towards smaller angles from recrystallization during annealing

4.3 Discussion: FE-SEM cross section profile of pre-aging Al sputter coated Cu interface

Figures 39 and 40 show a cross section interface of the as sputtered pre annealed sample. Figure 39 is a full SE image showing the as sputtered depth of the Al onto the Cu substrate at 1.83 μm with an oxide layer of ~0.8μm. Figure 40 is a mixed mode image of SE and BE in order to identify composition. The lower region should be Cu, and the brightness indicates an element heavier than the darker region. This is consistent with the difference in atomic weight of Al and Cu. The darker region is consistent with an element lighter than the lower brighter region, this would be the Al. The surface region has a brighter contrast. With BE image, this region should be darker than the Al region because oxygen (O) is lighter than Al. However, with this being a mixed mode image, the BE would be darker, but Al_2O_3 does not conduct the electron beam as well as the Al or Cu. The oxide layer will become charged with electrons and reemit

electrons with secondary energies after the scanning beam has passed instead of conducting them through to the ground. This will produce a brighter contrast[45].

The important characteristic of figures 39 and 40 for this study is the stark color change at the interface of the Cu and Al. There is no apparent diffusion zone that would be present in the form of a gradient of color if diffusion had occurred prior to aging. The second important characteristic is the interface of the Cu and Al cohesion. There are apparent voids present along the boundary. However, close inspection showed that the typical void was present in the vicinity of the interface, but was rarely a part of that boundary. Any cracking of the interface between the two metals was not present prior to aging.

After aging, the cross section FE-SEM EDS analysis of the 450°C aged sample shows an interface with angularity that could have been created by crack propagation due to interphase stress. Ion milling was employed to reveal the cross section to minimize the amount of post aging external stress applied. From the phase diagram, we see that γ_2 has a concentration range of 62.5 to 69 atomic % Cu with an ideal composition of 68.4 at. % Cu[8]. The EDS point composition targets, identified by a red plus sign in the sub pictures to the side (Figure 41), shows that the composition near the outer surface, and near the interface / interphase boundary falls within this region. This indicates a consistent composition of γ_2 phase above the boundary. α_2-phase begins to form above 69 atomic % Cu, with an ideal composition of 77.25 atomic % Cu and dissolving into pure copper at ~80.3 atomic % Cu[8]. In the EDS images with point composition markers just below the boundary (Figure 42), we see that the composition reflects the constituent amounts for α_2-phase.

4.4 Discussion: X-Ray Diffraction (XRD)

The XRD data is the key evidence in this study. The most important characteristic that it shows is the uniform asymmetric broadening of the left side of all the Cu peaks. The asymmetric nature of the shape indicates that it is not just the normal random quality such as residual stress, grain size or thermal agitation that can cause the broadening of a peak. All of those qualities distribute throughout the material and reflect in a peak as a Gaussian style distribution. Asymmetric implies that the structure is changing in a preferential fashion over a distance, a gradient. It is unlikely that the grain sizes are changing over a distance, it is unlikely that there is a gradient in temperature. The remaining factor is stress. The residual stress is accounted for in the amount of shouldering on the right side of the peak. Reflecting this line onto the left side of the peak and measuring the extra lateral distance from the centroid of the peak indicates an increase in the distortion of the lattice. This is a larger direction evident by rearranging and applying the Bragg's equation to the interplanar distance:

$$d_{hkl} = \frac{\lambda_{x-ray}}{2 \sin \theta_B}$$

We can see that intensities that decrease in 2θ create a larger interplanar distance, and the reverse for intensities to the right of a peak, increasing in 2θ. This indicates that there is an expansion of interplanar distance in the Cu. The atomic bonds have a limit that they can be stretched before breaking defined as the elastic modulus. Therefore, this expansion is elastic in nature.

The taper of the asymmetric shoulder to the left must be interpreted in reverse. The lowest intensity count is located at the largest interplanar distance. This should logically be located at the point closest to the boundary. The diffusion zone concentration is least at the furthest point away from the bimetal boundary. Therefore, as the intensities increase while

moving to the right from the largest interplanar distance, the location within the diffusion zone is moving away from the boundary into the bulk Cu.

The formation of what is called the α_2-phase is based on the new peaks that form uniformly to the left of all four Cu peaks. Calculating the displacement distance between these new peaks and their associated Cu peak shows an 1.26% isotropically expanded FCC lattice. These new peaks appears to have broadening due to either grain size, residual stress or temperature. Temperature is unlikely to be a contributor, and a new phase growing tends to be small grains growing into larger grains. The peak is broad from the onset dispelling the idea that the broadening is being contributed by grain size. This leaves residual stress. A completely unstressed, perfect crystal produces a single intensity line with no broadening. Therefore, a peak broadened by stress alone to the extent that these new peaks are broadened implies a great deal of stress in all directions. Using the calculating 1.26% isotropic expansion applied to the Cu lattice constant of 3.61Å we can find the lattice constant for the new peaks structure.

Table 5: Side Peak lattice expansion calculation

plane	Cu Peak 2-θ position	Cu Peak d_{hkl}(Cu) (Å)	Side peak 2-θ position	Side peak d_{hkl}(Cu) (Å)	Difference in d_{hkl} Cu-Side Peak (Å)	difference / d(Cu)
Cu(111)	43.316	4.89073	42.715	4.96	.0654505	1.34%
Cu(200)	50.419	4.23775	49.799	4.29	.0493583	1.16%
Cu(220)	74.124	2.99496	73.030	3.03	.0384523	1.28%
Cu(311)	89.919	2.55446	88.518	2.59	.0318505	1.25%
					Deviation	0.0002%
					Average	1.26%

The result is 3.655Å which is consistent with the values that Obinata and Wassermann[7] obtained for α2 phase. According to the revised phase diagram developed by Jewett6, as concentration of Al in Cu drops below the 31 at. % α2 phase will begin to develop and as the concentration continues to drop γ-phase will melt away.

Applying concepts of diffusion in IMC's proposed by Helmut Mehrer46, an IMC can be viewed as sub-lattices superimposed on one another. Using this system, specifically γ-phase as an example, the Cu sub-lattice with all of the locations of the Cu atoms within γ-phase and the Al sub-lattice with all of the locations of Al atoms within γ-phase. Within the 52 atom unit cell of γ-phase, there are (4 x 9) Cu atoms and (4 x 4) Al atoms. Al atoms are larger than Cu atoms. Through vacancy / atom substitutional diffusion, it is easier for a Cu atom to move through the lattice, than it is for an Al atom to diffuse through the lattice. An IMC can act as a diffusion barrier, however, this diffusion barrier has a different rate depending on the direction and type of atom attempting to move through the structure. By the details described here, it is our conclusion that the Cu diffuses into the γ-phase until the concentration of Al in the Cu drops below 31 at. % and conditions become favorable for the formation of what is being called α2-phase.

Beginning with the Hard vs Soft (pre-annealed) comparisons, in each of the different temperature zones, 300ºC (Figures 43 & 44), 350ºC (Figures 45 & 46), 400ºC (Figures 47 & 48), & 450ºC (Figures 49 & 50), the pre-anneal softened sample shows a greater amount of shouldering to the left hand side than equivalent work hardened samples. This indicates that in each of the cases, something in the work hardened material is reducing the amount of diffusion that occurs. Literature indicates that with the increased density of grain boundaries and dislocations present in a work hardened FCC material that diffusion should be accelerated19, 46.

Mehrer goes further to explain that grain boundary diffusion in bi-metal couples where IMC's are present are complex and a field in need of further study46. Other sources of literature indicate that in a diffusion couple that includes a radioactive Al isotope, the isotope was found to move into the Al lattice30. By majority of accounts, the work hardened material should show faster diffusion into the Al.

The γ (330) is the dominate peak representing the growth of the γ2 phase. This peak is located at 2θ 44.106°. Observation of the full 2θ range will reveal that there are 2 other peaks matching the γ2 phase as well. At 2θ 64.145° identifies with the γ (600) plane and 2θ 81.133° identifies with the γ (633) plane. The three peaks are most prevalent in the pre-annealed sample aged at 450°C. There is no indication of γ2 phase growth at 300ºC, but beginning at 350ºC the γ (330) peak begins to form. At 400ºC there is a very large growth of the γ (330) peak. The γ-phase peaks are narrower showing less residual strain / smaller grain size than the copper lattice it is growing in. At 450ºC the γ (330) peak is larger in the hard sample and smaller than the 400ºC peak in the pre-annealed sample. It should be noted at this point that in both of the 450ºC hard and pre-annealed graphs, the Al (111) and Al (200) peaks are completely flat. The pure aluminum at the surface has been dispersed to a degree that any related Al structure has intensities lost in the background range, implying very low quantity. Presumably all of the Al is now within the Cu lattice as either solid solution, γ2 phase or potentially α2-phase. In the 450ºC soft sample, the γ (330) peak begins to shrink and the α2 peak has grown significantly. Whereas in the half-hard sample, the γ (330) peak is still growing. The kinetics of γ-phase formation are clearly trailing the kinetics in the pre-annealed sample.

As supplemental information to fully explain the data presented, the 350ºC Hard sample has a peak at ~36.4º 2θ. This peak is consistent with ICDD data on copper oxide (CuO). This

particular sample had a fair amount of aluminum thin film detachment from the Cu. This sample apparently had built up an oxide layer on the surface that appeared in the diffraction data.

Chapter 5

Conclusions

A series of experimental investigations on the interface reaction, using Cu plate coated with Al thin films, leads to the following conclusions. These conclusions shed light on the reliability / failure mechanisms of the Al-Cu wirebond structure. Our investigation finds that the copper lattice is being expanded by stress during the formation of γ-phase (Cu9Al4). This is evident by the uniform asymmetric left shoulder expansion of the copper peaks in the XRD data at all temperatures. The primary IMC peak, γ (330), grows proportionally to the left shouldering of the Cu peaks. Therefore, we conclude that the growth of the Cu rich γ-phase IMC may be associated with larger Al atoms entering the Cu FCC lattice. This model would allow for a coherent interphase boundary to be maintained. This would be energetically favorable to a system for a smaller volume free energy without having to create a new interphase surface. As the larger Al atoms enter Cu site locations in the Cu FCC lattice, interplanar distances are expanded to accommodate the larger atom. During the fastest γ-phase development (temperature, 400° C in the pre-annealed sample), it is observed that the γ (330) peak shifts to the right by a proportional amount that the centroid of the Cu (111) peak shifts left. This indicates that the interplanar distance of the γ (330) peak is being compacted closer together while the Cu (111) plane is being expanded. When the composition is favorable for the formation of γ-phase, lattice stress can be relieved by forming the closer packed (77% APF γ-phase vs 74% APF FCC-Cu). The formation of γ-phase introduces a diffusion barrier that favors the diffusion of Cu in the direction of Al. This condition presents the opportunity for the formation of α2-phase as Cu enters the γ-phase lattice. Also at 400° C on the pre-annealed sample, a small left shoulder on the γ (330) peak can be observed along with the beginning rise of a peak for Cu-α2 (111). At

450° C this left shoulder of γ (330) becomes slightly increased as the Cu-α2 (111) peak increases considerably. This indicates an expansion of the γ (330) plane as the Cu-α2 (111) plane is formed.

The initial formation of θ-phase does not occur as literature predicts23, 29. Literature reports are based on systems of TF/TF and B/B diffusion couples. We conclude that the difference originates from the fact that our experiment is based on a thin-film / bulk (TF/B) diffusion couple. By the data collected in our experiment, it is possible that θ-phase formed and transformed into γ-phase as some literature predicts29. Further experiments with temperatures and times closer together may be able to confirm this. It is also possible that θ-phase never forms due to a dominant diffusional mechanism present in the TF/B couple that is not in the TF/TF and B/B couples.

The lower vacancy concentration in work-hardened Cu inhibits the formation of γ-phase. Comparison of XRD data between work-hardened samples and annealed samples shows remarkably lower expansion of Cu lattice and growth of the γ-phase structure. Therefore, we conclude that residual stress in the work-hardened Cu lowers the equilibrium concentration of vacancies present, slowing substitutional diffusion mechanisms. Cu plate that has been annealed prior to sputtering and aging shows a significant reduction in residual stress by the optical micrography, SEM-EBSD and microhardness data. The increase in lattice expansion and IMC γ-phase formation in a less residual stress sample would then indicate that its formation kinetics are linked to the vacancy resources available.

Applying these conclusions to the Cu wire Al bondpad wirebond, we observe work hardened and non-work hardened Cu is present. The wirebond process melts a small amount of Cu at the tip of the bonder to form a ball. This ball is allowed to cool and is then pressed into

place on the Al bondpad before completely cooled. Pressure from the tip is centralized in a ring around the center z axis of the ball but does not extend to the edge. This creates an outer ring that has no work hardening, around a ring of work hardened Cu around a central region with intermediate amounts of work hardening. We observe that failures in this wirebond typically originate at the outer edges and work their way inward. We conclude that the non-work hardened Cu at the edges allows for the rapid development of IMC that has mechanical characteristics that contribute to the nucleation of cracks and voids at the outer edges of the wirebond. Once nucleated, these failure mechanisms translate through the interface to cause failure.

References

[1] Yu, Cheng-Fu, Chi-Ming Chan, Li-Chun Chan, Ker-Chang Hsieh. "Cu wire bond microstructure analysis and failure mechanism. Microelectronics Reliability." 51(119-124(2011). *Figure 1 pic.*

[2] Simon, N.J. E.S. Drexler, R.P. Reed. "Properties of copper and copper alloys at cryogenic temperatures." NIST Monogr. pp. 176–177(1992). . copper elements quanta

[3] *CRC Handbook of Chemistry and Physics,* 84th Ed.; D.R Lide Ed.; CRC Press: Boca (2003).

[4] Murray, J.L. "Al-Cu (Aluminum-Copper)." International Materials Reviews. V. 30,1. Pp. 211.234 (Jan. 1985). Cu-Al phase diagram and IMC details.

[5] Massalski, T. B. "The Al-Cu (Aluminum-Copper) system. Bulletin of Alloy Phase Diagrams." V.1. I.1. pp. 27-33 (March 1980)

[6] R. P. Jewett and D. J. Mack, "Further Investigation of Copper-Aluminium Alloys in the Temperature Range below the $\beta \leftrightharpoons \alpha + \gamma_2$ Eutectoid." J. Inst. Metals, 92, 59(1963)

[7] Obinata, I and G. Wassermann, "X-Ray study of the Solubility of Aluminum-Copper," Naturwissenschaften, 21, 382-385 (1933) in German. (Equi Diagram, Crys Structure; Experimental) *Alpha Phase lattice constant*

[8] *Phase Diagrams of Binary Copper Alloys*. Editors: P.R. Subramanian, D.J. Chakrabarti, D.E. Laughlin. pp. 31(1994)

[9] Daams, J.L., C. Villars, P. van Vucht, J.H.N. *Atlas of Crystal Structure types for Intermetallic Phases Vol.3*. ASM International. (1991)

[10] Mizutani, Uichiro. "Hume-Rothery Rules for Structurally Complex Alloy Phases." Taylor & Francis. (February 2010).

[11] Fick, Adolf. "On liquid diffusion". Phil. Mag. Series 4. Vol. 10. Issue 63. pp. 30-39 (1855).

[12] Shewmon, P. G, *Diffusion in Solids, McGraw-Hill,* New York, 1963,

[13] McQueen, J. W. J. Hugh, Tegart McGregor. "The deformation of Metals at High Temperatures". Sci. Am., 232[4]. (1975). pp. 116-125δ is a rhombohedral distortion of the γ2 phase –

[14] McQueen, H. J. The experimental Roots of Thermomechanical Treatments for Aluminum Alloys. Journal of Metals. Pp. 17-27 (February 1980). *Process of hot rolling with concepts in dynamic recovery and dynamic recrystallization.*

[15] Dieter, George E. *Mechanical Metallurgy. McGraw-Hill,* New York. 1961

[16] Doherty, R.D., D.A. Hughes, F. J. Humphreys, J. J. Jonas, D. Jensen, Juul. Kassner, M. E. King, W. E. McNelley, T.R. McQueen, H. J. Rollett, A. D. "Current issues in

recrystallization: A review. Materials Science and Engineering". Elsevier. A238. pp. 219-274 (1997). *Recrystallization.*

[17] Porter, David, A. Kenneth, E. Easterling, Mohamed Y. Sherif. *Phase transformations in Metals and Alloys 3rd ed.. CRC Press.* Boca Raton, FL. 2009

[18] Chadwick, G. A., D. A. Smith. *Grain Boundary Structure and Properties. Academic Press.* New York, NY. 1976.

[19] Balluffi, Robert W., Samuel M. Allen, W. Craig Carter. *Kinetics of Materials. Ed. Rachel A. Kemper. Wiley-Interscience.* Hoboken, NJ. 2005. *Excellent reference for various diffusion potentials, most specifically stress diffusion.*

[20] Tiwari, G. P. R., S. Mehrotra. "Kirkendall effect and Mechanism of Self-Diffusion in B2 Intermetallic Compounds". The Minerals, Metals & Materials Society and ASM International 2012. V. 43A. pp. 3654-3662 (October 2012). *One suggested mechanism for failure. Lacks vacancy supersaturation condition*

[21] A. D. Smigelskas and E. O. Kirkendall, Trans. AIME, volume 171, 1947, p. 130.

[22] Kouters, M.H.M., G.H.M. Gubbels, O. O'Halloran, R. Rongen, E.R. Weltevreden. "Mechanical properties of intermetallics formed during thermal aging of Cu-Al ball bonds." EuroSimE2011. IEEE conference. 2011. *Mechanical properties of gamma phase.*

[23] Hang, C.J., C. Q. Wang, M. Mayer. Y.H. Tian. Y. Zhou. H.H. Wang. "Growth behavior of Cu/Al intermetallic compounds and cracks in copper ball bonds during isothermal aging". Elsevier-Microelectronics Reliability. V.48. pp. 416-424 (2008). *Picture of failure development in the Cu-Al wirebond*

[24] Jannot, E. V., G. Mohles, B. Gottstein, Thijsse. "Atomistic Simulation of Pipe Diffusion in AlCu alloys". Trans Tech Publications. Defect and Diffusion Forum. Vol 249 pp. 47-54 (2006)

[25] Grjaznovs, Deniss. "Simulation of Diffusion in Nanocrystalline Materials: Continuum Approach". Disertation - Max Planck Institute for Solid State Research, Stuttgart, DE. 2006

[26] Lloyd, James R. "Reliability of Copper Metallization." www.nepp.nasa.gov. #524 (1992)

[27] M. Braunovic and N. Aleksandrov, "Effect of Electrical Current on the Morphology and Kinetics of Formation of Intermetallic Phases in Bimetallic Aluminum-Copper Joints", Electrical Contacts, Proc.of the 39th IEEE Holm Conference on Electrical Contacts, Pittsburgh, 1993, p. 261(1993).

[28] Wei, Tan Chee, Abdul Razak Daud. "Mechanical and Electrical Properties of Au-Al and Cu-Al intermetallics layer at Wire Bonding Interface." Journal of Electronic Packaging. ASME Vol. 125 pp. 617 (2003). Comparison of Gold to Copper for metallization of wirebonds.

[29] Haidara, Fanta, Marie-Christine Record, Benjamin Duployer, Dominique Mangelinck. "Investigation of reactive phase formation in the Al-Cu thin film systems." Surface & coatings Technology. 206. pp.3851-3856 (2012). *In-situ TF/TF XRD sequence study.*

[30] Kirkaldy, J. S., G. Savva. "Correlation between coherency strain effects and the Kirkendall effect in binary infinite diffusion couples." Acta. Mater. V.45(8). pp.3115-3121.(1997).

[31] A.E. Gershinskii, B.I. Fomin, E.I. Cherepov, F.L. Edelman, Thin Solid Films 42 (1977) 269.

[32] S.U. Campisano, E. Cosranzo, F. Scaccianoce, R. Cristofolini, Thin Solid Films 52 (1978) 97.

[33] K. Rajan, E.R. Wallach, J. Cryst. Growth 49 (1980) 297.

[34] H.G. Jiang, J.Y. Dai, H.Y. Tong, B.Z. Ding, Q.H. Song, Z.Q. Hu, J. Appl. Phys. 74 (1993) 6165.

[35] J.M. Vanderberg, R.A. Hamm, Thin Solid Films 97 (1982) 313.

[36] H.T.G. Hentzell, R.D. Thompson, K.N. Tu, Mater. Lett. 2 (1983) 81.

[37] H.T.G. Hentzell, R.D. Thompson, K.N. Tu, J. Appl. Phys. 54 (1983) 6923.

[38] T.B. Massalski, Binary Alloys Phase Diagrams, 2nd Edition American Society for Metals, Materials Park (Ohio), 1990.

[39] F.A. Calvo, A. Urena, J.M. Gomez De Salazar, F. Molleda, J. Mater. Sci. 23 (1998) 2273.

[40] C.-Y. Chen, W.-S. Hwang, Mater. Trans. 48 (2007) 1938.

[41] Y. Guo, G. Liu, H. Jin, Z. Shi, G. Qiao, J. Mater. Sci. 46 (2011) 2467.

[42] C.J. Hang, C.Q. Wang, M. Mayer, Y.H. Tian, Y. Zhou, H.H. Wang, Microelectron. Reliab. 48 (2008) 416.

[43] A. Markwitz, W. Matz, M. Waldschmidt, G. Demortier, Surf. Interface Anal. 26 (1998) 160.

[44] U. Goesele, K.N. Tu, J. Appl. Phys. 53 (1982) 3252.

[45] Leng, Yang. *Materials Characterization: Introduction to Microscopic and Spectroscopic Methods.* John Wiley & Sons. Singapore (2008).

[46] Kozubski, R. *Recent Progress in Diffusion Thermodynamics and Kinetics in Intermetallic Compounds.* Trans Tech Publication. Diffusion Foundations Volume 2 (2014).

Biographical Information

In 2012 Codie Mishler received the National Science Foundation funded Arlington Community College Exceptional Scholars Scholarship (ACCESS) to participate in a Material Science Fast-Track program at The University of Texas at Arlington. The program comprised an undergraduate degree in physics where he would take graduate level courses in material science as the minor portion of the program. He completed his bachelor of science in physics in 2014. Meeting the academic requirements for the fast-track program and the scholarship, he entered the graduate portion of the program and completed the requirements for a master's of science in material science & engineering in 2015.

During his tenure as a graduate student, he personally conducted three different investigations, and assisted with three other investigations in the lab. His primary interest is investigations to determine material failure. His research was focused in the area of metallurgy in electronic devices.